

MSc. Applied Physics  
Thesis

---

**Development and validation of clinically feasible  
4D-MRI in radiotherapy**

---

Daniel Tekelenburg



By:

Daniel Ruphay Tekelenburg

In partial fulfilment of the requirements for the degree of

**Master of Science**  
in Applied Physics

at

The University of Groningen

**Supervisors:**

Amsterdam: Dr. Z. van Kesteren, Dr. T. Alderliesten & Dr. A. Bel  
Groningen: Dr. A.K. Biegun

# Contents

<b>I</b>	<b>Theory and background</b>	<b>4</b>
1	Radiation Oncology	4
1.1	Cancer & cancer treatment . . . . .	4
1.2	Radiotherapy treatment . . . . .	5
1.2.1	Pre-treatment imaging . . . . .	6
1.2.2	Treatment planning . . . . .	8
1.2.3	Position verification and radiation delivery . . . . .	9
2	Uncertainties in radiotherapy treatment	11
2.1	CTV-PTV margin calculation . . . . .	14
2.2	Sources of uncertainty . . . . .	14
2.3	Respiratory motion management . . . . .	16
2.3.1	4D-CT acquisition . . . . .	17
2.3.2	4D-CT artefacts . . . . .	17
3	Magnetic Resonance Imaging	20
3.1	Basic MRI physics . . . . .	21
3.1.1	Spins in a magnetic field . . . . .	21
3.1.2	Measuring the spin-echo . . . . .	22
3.2	Image acquisition and reconstruction . . . . .	23
3.2.1	Relaxation time . . . . .	23
3.2.2	The spin echo sequence . . . . .	25
3.3	Spin echo optimization . . . . .	27
3.3.1	The turbo spin echo sequence . . . . .	29
3.3.2	Respiratory motion in MRI . . . . .	30
<b>II</b>	<b>Research</b>	<b>33</b>
1	Introduction	33
2	Methods	36
2.1	Image acquisition . . . . .	36
2.2	Retrospective sorting of images . . . . .	37
2.3	Phase & Amplitude binning . . . . .	38
2.4	4D data set reconstruction . . . . .	39
2.5	Analysis . . . . .	41

3	Results	45
3.1	Variability of diaphragm position . . . . .	45
3.2	Respiration induced diaphragmatic motion . . . . .	46
3.3	Diaphragm shape . . . . .	47
3.4	Data completeness . . . . .	49
4	Discussion	51
5	Future outlook	57
6	Conclusion	58
	References	59
	Appendix A Manual	62
	A.1 At the scanner . . . . .	62
	A.2 4D-MRI reconstruction program . . . . .	63
	Appendix B Program	67
	B.1 Tekelenburg4DMRI.m . . . . .	67
	B.2 fyslog.m . . . . .	70
	B.3 Binning . . . . .	71
	B.3.1 AmpliBin_onlynav.m . . . . .	71
	B.3.2 PhaseBin_onlynav.m . . . . .	76
	B.3.3 binImages.m . . . . .	79
	B.4 Selectmedian.m . . . . .	80
	B.5 Rigid registration program . . . . .	82
	B.6 Analysis programs . . . . .	84

## **Acknowledgements**

Here it is, my thesis with the title: 'Development and validation of clinically feasible 4D-MRI in radiotherapy'. I am proud to present my work I carried out during my master research project at the AMC. I would never have succeeded in fulfilling the goals I have set without the help, support, approval and guidance I received during the past 10 months.

In the first place I would like to thank my first supervisor dr. Zdenko van Kesteren for guiding me during my research at the AMC. It was for me a big step to leave Groningen and start to do research in a clinical environment. I am grateful for the time you took to guide me through this process. I am especially thankful for the weekly discussion we had, they taught me a lot of the important considerations which are needed when working in a clinical setting. Finally, I am happy with your critics on my research, abstracts, poster and this thesis. Without it, I would not be as satisfied with the results we obtained and I feel proud that you are going to present my work at ISMRM congress in Singapore.

Next, I would like to thank dr. Aleksandra Biegun of the KVI - Center for Advanced Radiation Technology. Without her approval I could not have gone to Amsterdam to start my research at another institution. She also kindly agreed to be my second supervisor and was always willing to spend time and effort to answer my questions. Especially her willingness to travel to Amsterdam to visit me and my project was very fruitful and I am grateful for this. I would like to thank the department of radiation oncology and especially the researchers which gave me assistance, inspiration and guidance. Especially the weekly research meeting 'Research Methods and Techniques' added valuable insights to my research. I would like to thank Oliver Gurney-Champion for showing me the world of the MRI and for always be available to discuss sequences and optimization parameters with me.

Thank you all for your support and time.

## Part I

# Theory and background

The goal of my research is to improve imaging for radiation therapy at the department of Radiation Oncology at the Academic Medical Center (AMC) in Amsterdam. The research is dedicated to improve treatment by using the established Magnetic Resonance Imaging (MRI) modality in a radiotherapy context. This thesis is divided in two parts where part I gives the reader information and insights needed to understand the research described in part II. Part I explains general radiation oncology and the radiotherapy workflow. Also, the motion management of tumors is discussed as well as MRI physics.

## 1 Radiation Oncology

My research at the AMC was carried out at the department of Radiation Oncology. This is a department with a medical specialty concerned with the treatment of cancer patients with radiation. The main research theme of the AMC Radiotherapy group includes adaptive image-guided radiotherapy and motion management of mobile tumors. The purpose of my research was to use the advantages of magnetic resonance imaging (MRI) for the benefit of pancreatic radiotherapy treatment. The focus of my research is to improve the visibility of the pancreas in combination with the quantification of respiration induced motion. This research is carried out in a project group that consists of a multi-disciplinary team of researchers, clinical physicists and physicians.

### 1.1 Cancer & cancer treatment

Cancer was in 2014 the main cause of death in the Netherlands. More than 30% of all deaths was related to a type of cancer and for the age category of 45 to 65 years, more than 50% had cancer-related death [1]. There are innumerable types, shapes, classes and sorts of cancer. However, they all have one property in common; human body cells grow in an uncontrollable matter due to mutation in the genome. When left untreated, some cancers can show excessive growth and can invade organs or spread to other parts of the body. Patients diagnosed with cancer in the the Netherlands have an overall 5-year survival rate of 60% [2]. The cause of death by cancer has various reasons, but it is mostly the consequence of the spread of cancer cells to other parts of the body, so-called metastases. These metastases can affect vital organs or physiological functions causing the patient to die. For example, cancer can grow into the digestive system blocking the intestines, which will inhibit food to pass through preventing the absorption of essential nutrients.

The treatment that follows diagnosis has undergone rapid evolutionary changes during the last few decades. Treatment research is still an active field covering mostly all disciplines in nature and life sciences. The reason for this multidisciplinary approach

are the vast options for treatment and the different and complicated characteristic of tumors.

The three major types of treatment are surgery, systemic therapy (such as chemotherapy, hormone therapy, targeted therapy, and immunotherapy) and radiation therapy [3].

The goal of surgery is to remove the bulk cells present in the body. This can be achieved by removing only the tumor mass or by removing the total organ if there are indications of a microscopic spread of tumor cells. It is not always possible to remove all tumor cells. Tumors can be localized next to vital organs, vessel structures, and nerves. Even nonvisible cells could have spread and such microscopic cells can result in recurrences. Metastatic tumors are often impossible to remove surgically and a combination with systemic therapy or radiation therapy is often required.

Systemic therapy is the treatment of cancer with drugs that destroy or inhibit growth of tumor cells. There are several types of drugs suitable for systemic therapy where each has its own working mechanism. Commonly used drugs are so-called cytotoxic drugs which affect rapidly dividing cells. This type of therapy, known as chemotherapy, interfere and target cell division of all rapidly dividing cells including tumors and healthy cells. The non-specificity leads to harm of healthy tissues, especially those tissues that have high division rates. The development of more advanced techniques has led to drug types that target specifically the deregulated proteins of cancer cells.

The last major type of treatment is radiation therapy or radiotherapy (RT). This type of therapy uses ionizing radiation to target tumor cells. There are two methods to deliver ionizing radiation to the tumor: internal radiation and external radiation. Internal radiation known as brachytherapy inserts sealed sources of radiation next to the target. External radiation or external beam radiotherapy (EBRT) uses external beams of radiation to target tumors inside the patient. The focus of this thesis will be solely on EBRT. High energy photons are mostly used in EBRT, but particles with mass like protons, carbons and electrons are also used in this field.

The working principle of radiation therapy is to damage the DNA of cancer cells with ionizing radiation. Ionization of the base pairs that make up the DNA chain causes irreparable damage that leads to cell death or apoptosis, i.e. cellular suicide. Radiotherapy is non-invasive and it is often used for patients where surgery or chemotherapy is not possible. However, for most cancer types the three treatment methods are often used in combination with one another. For example, after surgical removal of a tumor, radiotherapy can be used to treat lymph node metastasis at the resected tumor site. Also, combinations of chemotherapy and radiotherapy are common practice [4].

## **1.2 Radiotherapy treatment**

Radiotherapy is used in approximately half of the cancer patients. Radiation treatment normally consists of one planning session and multiple irradiation sessions. Radiation also harms healthy tissues, one has to be careful to deliver most of the radiation dose to the right place. Even when very accurate methods are used, it is inherent to EBRT to damage healthy tissues since the tumor is surrounded by healthy

tissues inside the body.

Healthy tissues recover more efficiently from radiation damage than tumor cells, this is the reason that radiotherapy treatments are often divided into several fractions spread out over days or even weeks. In between fractions (delivery of ionizing radiation), the healthy tissues are given time to recover from a previous fraction.

Before the start of the treatment the radiotherapy team at the department plans the external radiation treatment. The team needs to determine how much radiation is needed to treat the cancer and where the radiation should be delivered.

For a correct plan the tumor location, surrounding organs, and type of treatment have to be determined. This is done by pre-treatment imaging. Pre-treatment imaging acquires anatomical images to determine the target volume. This is followed by a step where the dose distribution is calculated inside the patient to determine a treatment plan for delivery. Finally, at delivery, the treatment plan is executed at the treatment site.

During all the steps in this radiotherapy treatment chain, the main goal is to plan, model and deliver the prescribed dose to the target volume while avoiding the damage to healthy tissues as much as possible.

### **1.2.1 Pre-treatment imaging**

Accurate patient treatment is only possible when sufficiently accurate patient imaging is obtained. Such images contain data that includes the body contour, location and electron density of relevant structures, and the location and extent of the target volume. Images can be acquired with different modalities including computed tomography(CT), magnetic resonance imaging (MRI), ultrasound and positron emission tomography (PET).

The images obtained during pre-treatment imaging are used as model of the patient for treatment planning and delivery. The model obtained from the images should be reproducible during treatment planning and during all treatment fractions. Therefore, pre-treatment imaging requires high-quality images together with special considerations such as patient positioning and geometrical accuracy. The patient should be positioned during pre-treatment imaging in exactly the same way as during treatment. This is achieved by using immobilization devices together with a positioning laser. The calibrated lasers present both in the treatment room and the CT-room are combined with small permanent markers tattooed on the skin to allow for reproducible patient positioning.

#### **CT-imaging**

Computed tomography is the most used imaging modality in current radiotherapy planning. The strengths of CT in the context of radiotherapy are its geometrical accuracy, imaging speeds, widespread availability, and applicability to all patients.

CT images are taken from the patient and used in twofold. First, the target volume can be delineated in relation to the surrounding healthy structures and the external

contour. The delineation of structures have a very high impact on treatment planning and outcome [5]. Second, an electron density map can be derived from the CT images which can be used to enable accurate dose calculations.

CT uses X-rays to produce multiple image slices through selected parts of the body. Basically, a narrow beam of x-rays scans across a patient in synchrony with a radiation detector on the other side of the patient. If a sufficient number of transmission measurements are taken at different orientations, the distribution of attenuation coefficients within the slice may be determined.

The resulting images consist of pixels in different gray values, see figure 1 for a typical CT image from the abdomen. As the slice thickness is finite (for example 1 mm), each pixel represents a three-dimensional (3D) volume in the patient called a voxel [6].



**Figure 1:** A typical CT of the abdomen obtained at pre-treatment imaging. High attenuating bone has very large intensities while air results in black pixels.

The CT images consist of a range of intensities depicting different tissue types based on their attenuating properties. The acquired range of X-ray absorption cannot directly be turned into binary images because each data acquisition consists of multiple projections. Complicated reconstruction algorithms are implemented to obtain the desired images. These reconstruction algorithms generate what is known as CT numbers, a number related to the attenuation coefficients. The CT number range is normalized to the attenuation coefficient of water and the resulting units are called Hounsfield Units (HU). A HU represents a change of 0.1% in the attenuation of water. Logically water has a value of 0 HU, the values for high attenuating cranial bone is +1000 HU while air has a value of -1000 HU.

The contrast in the CT images is thus acquired due to differences in attenuation.

This relationship between HU and attenuation coefficients makes it possible to calculate the electron density of the tissues.

Accurate delineation of surface contours, internal structures, and the target volume is needed for optimizing a treatment technique. Together with the electron density map it is necessary for accurate calculation of dose distributions in the patient. The most severe errors in computing the dose distribution arise from the inaccurate delineation of the geometric outline of tissue [7]. Determination of an accurate body contour is very important for calculating the dose distribution in the patient.

### 1.2.2 Treatment planning

Radiotherapy treatment planning is the process in which a team of physicians, RTTs, and dosimetrists plan the appropriate external beam treatment technique in order to deliver the desired dose distribution in and around a target volume.

From pre-treatment imaging, CT images are obtained together with the delineation of target volumes, organs at risk and other important structures. These typically cross-sectional images are used to create a virtual patient model as the basis for subsequent computer assisted treatment design. The next step is to design a treatment plan that delivers the prescribed dose to the target.

The target dose to the tumor is prescribed by the physician. The (absorbed) dose  $D$  is simplified :

$$D = \frac{dE}{dm} \quad (1)$$

where  $D$  is the dose in gray (Gy) and  $E$  the mean energy imparted to a mass  $m$ . The prescribed dose is the amount of photon energy that should be deposited by radiation to the target volume.

The objectives of a treatment plan is to deliver maximum dose to the tumor and minimize dose to the surrounding organs and healthy tissues. In addition, dose uniformity within a tumor is an important consideration in treatment plan preparation. The optimization of the treatment plan requires a good design of beam directions, number of fields, beam arrangements and intensity modifiers.

It is important to realise that it is often hard to deliver a high dose to the target and simultaneously spare the healthy tissues and organs at risk. Especially when tumors are located close to radio-sensitive organs the design of a treatment plan can be challenging due to conflicting constraints. The resulting plan, often generated by an interplay of the treatment planner and sophisticated algorithms, is consequently iterated until a clinically acceptable plan is obtained. An optimal plan is hard to obtain as several beam configurations, dose depositions, and constraints all influence each other.

These considerations cause a treatment plan to be a trade-off of competing goods and make it challenging to find the most optimal plan. The goal is therefore to create a clinically relevant plan where the tumor receives the prescribed dose while the organs at risk and healthy tissues are damaged as little as possible. Finally, it is important to realize that the acceptability of a treatment plan depends not only on the dose

distribution on paper but also on practical feasibility (e.g number of beams, modifiers and radiation delivery specifications) and robustness of each technique.

### **1.2.3 Position verification and radiation delivery**

After treatment planning, the actual treatment takes place and the ionizing radiation can be delivered to the patient in multiple treatment fractions. To deliver the acquired treatment plan the patient has to be positioned exactly as during pre-treatment imaging.

#### **Position verification**

The positioning of the patient is executed by using the earlier mentioned laser guided systems and immobilization devices. The patient is positioned similar to the position used for pre-treatment imaging. See figure 2 for an example of immobilization devices on the treatment table. Still, the position of the tumor can deviate from day to day because of anatomical changes like mobile skin surfaces, patient weight loss or mobile organs and tumors.

Therefore, after the external positioning of the patient, verification of the setup is often achieved using on-line (at the treatment table) imaging verification. The on-line image acquisition is often done with a technique called cone-beam CT (CB-CT). This technique is similar to the CT. However, the acquisition is done using a dedicated x-ray source at the gantry of the treatment machine with a divergent cone shaped beam. This technique makes it possible to acquire in less than a minute a 3D-volume of the patient at the treatment table. The difference between internal anatomy at the treatment table with that from treatment planning is determined by matching the cone beam image to the treatment planning CT using landmarks. These landmarks can be anatomical structures like bones or implanted gold fiducial markers. The feedback of the match is used to correct patient positioning by moving the the treatment table in three cardinal directions.

#### **Treatment delivery**

After setup verification the patient can start the treatment fraction. Delivery of the radiation beam is performed by a linear accelerator (LINAC). Figure 2 shows a modern LINAC machine together with the treatment table.

The LINAC creates radiation beams which can be directed to the patient lying on the treatment table. The gantry is a LINAC mounted to a rotating platform, see figure 2. The gantry can rotate all around the patient making it possible to treat the patient from different angles.

The LINAC can deliver photon and electron beams. As the focus of this thesis is on photons, we will not elaborate on electron radiation. The photon beams are created in the LINAC by the acceleration of electrons impinging on a high-density target (like tungsten). The electrons are created inside the LINAC by a cathode which is heated by passing a very high current trough it. This process called thermionic emission creates free electrons which are accelerated to a velocity approaching the speed of light. The accelerated electrons hit the tungsten target and interact with it by emitting radiation

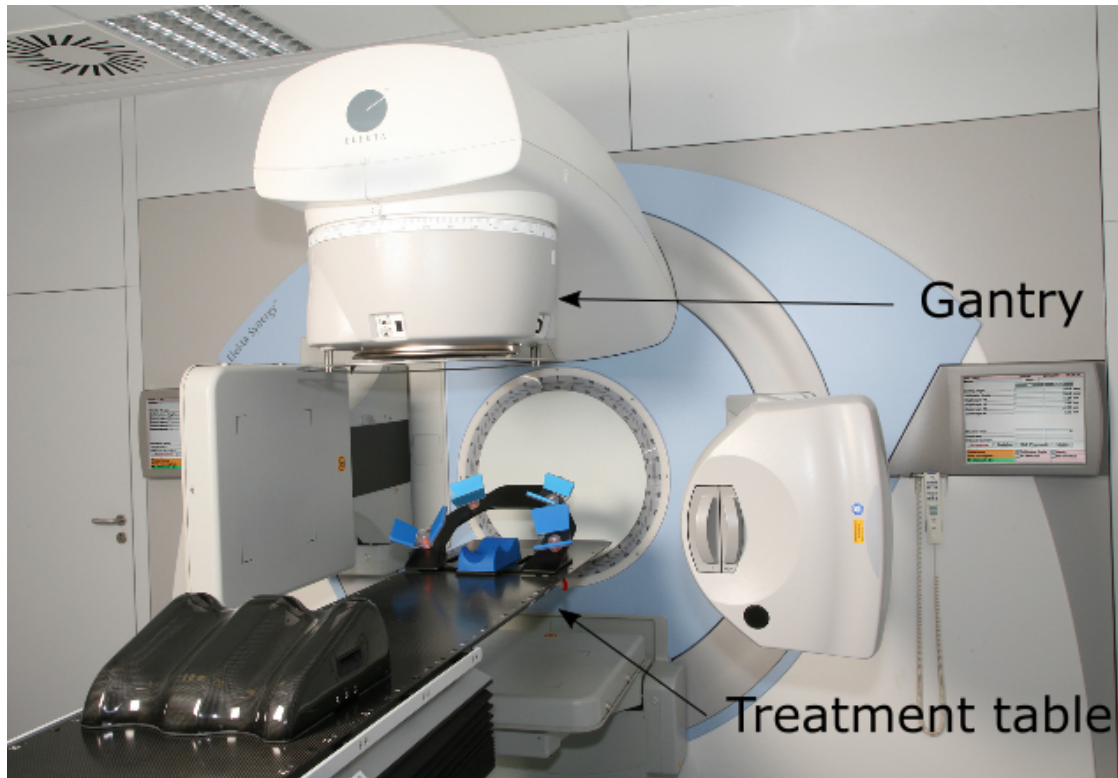


**Figure 2:** A linear accelerator (LINAC) (Electa, Crawley United Kingdom) used during radiotherapy treatment delivery. The immobilization devices on the treatment table ensure external position verification.

via characteristic x-rays and bremsstrahlung.

Figure 3 shows a representation of an x-ray spectrum where the number of photons are plotted to the photon energy ( $h\nu$ ). The continuous shape of the plot is due to Bremsstrahlung radiation, the release of a photon due to deceleration of the high energy electrons. The photon is created by the deflection of the electrons path due to the positively charged tungsten atomic nuclei. The superimposed discrete lines are characteristic x-rays of tungsten. These x-rays are due to the ejection of a core level electron by the charged particle. The core level hole is filled by an outer shell electron emitting a photon. This photon has discrete energy states as the photon energy is the difference between the energy state of the outer shell and the inner shell electrons [8].

The energy spectra of radiation always are heterogeneous. However, the quality of the beam is often quite high due to inherent filtration of the tungsten target combined with the usage of a flattening filter. This filter, with the primary purpose to make the beam intensity homogeneous, also improves the beam quality (less dispersed energies) leading to sufficiently high-quality beams suitable for patient treatment [9].

The current linear accelerators are capable to deliver conformal doses to a spatial location. Since the introduction of a multileaf collimator (MLC) the shape of the

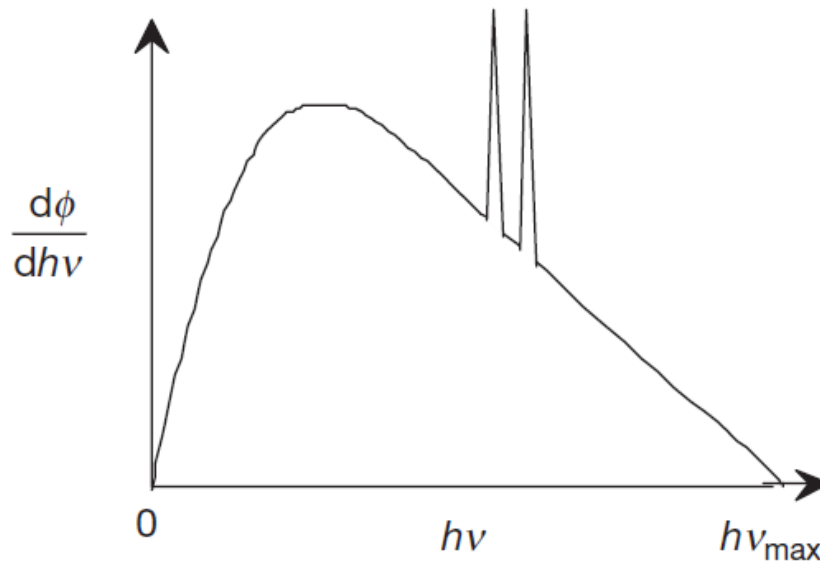


**Figure 3:** Schematic representation of a x-ray energy spectrum showing the number of particles incident ( $\frac{d\phi}{dh\nu}$  with  $\phi$  the particle fluence) as function of the energy ( $h\nu$ ). The continuous distribution of energies of bremsstrahlung photons are superimposed by discrete lines of characteristic radiation. Reprinted from [8].

treatment beam can be adjusted [10]. This device, see figure 4 is made of multiple high atomic number leaves that can individually move into the treatment beam and so provide conformal shaping of the beam. This can lead to conformal radiotherapy where the shape of the beam is adjusted to the target volume. Moreover, accurate MLC control allow for intensity modulated radiation therapy (IMRT) planning. IMRT is a radiation treatment technique that modulates the beam in such a way that intensity modulated dose distributions are possible in the patient. These advances in LINAC design are used to irradiate a target tumor with higher precision and an accurate dose distribution, potentially improving treatment and reducing dose to the organs at risk. However, precise delivery of conformal and intensity modulated beams require even better precision in tumor delineation and handling of the various uncertainties in the radiotherapy treatment chain. The need for safety margins and minimizing of these uncertainties is a paramount in modern radiotherapy.

## 2 Uncertainties in radiotherapy treatment

All stages in the radiotherapy treatment chain are complicated processes and every step in the process has a potential for error. These uncertainties can affect the treatment and treatment outcome causing insufficient radiation dose coverage of the target tumor and an overdosage of normal tissues. These uncertainties are generally handled by applying safety margins during treatment preparation.

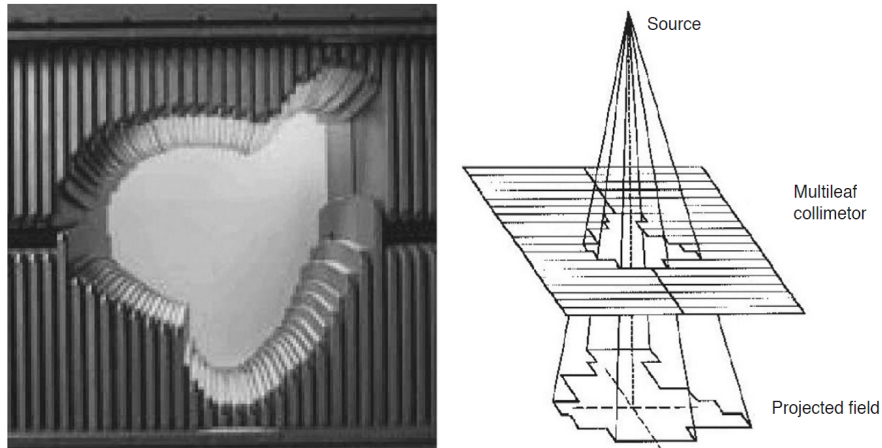


**Figure 4:** A front view of the multileaf collimator (left) and a schematic representation of its function (right). A beam can be adjusted and shaped using the multiple, independently moving leaves. Reprinted from [11].

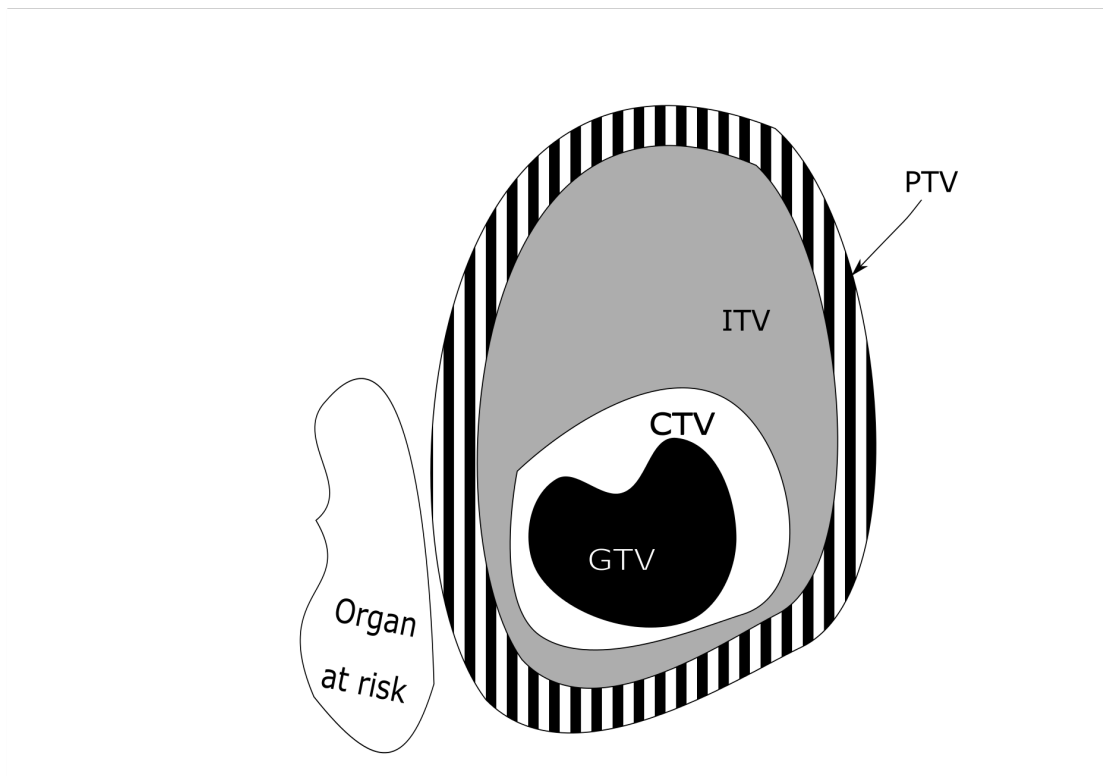
### Safety margins

Figure 5 shows an illustration of the safety margins applied during radiotherapy. The GTV is the delineation of the gross demonstrable extent and location of the tumor as seen on the imaging modalities. As subclinical microscopic malignant cells are not visible on these images an extra margin is added. In some directions, this margins can be limited due to anatomical boundaries like bony structures. This anisotropic margin added to the GTV results in the clinical target volume (CTV). The CTV is the volume that should receive the prescribed dose for proper treatment of the tumor.

To account for target motion, it is recommended that a margin is added to compensate for internal physiological movement and variation in size, shape, and positioning of the CTV. The irradiated volume including these 3D margins for internal uncertainties is called the internal target volume (ITV).

The last margin is applied to cover all remaining geometrical uncertainties. This margin is added to account for patient movement, geometrical uncertainties related to the treatment positioning, linac uncertainties, ambient conditions, delineation uncertainties and much more. The final volume used for treatment planning is the ITV with an added margin, this volume is referred to as the planning target volume (PTV). The final PTV, which is population based, is the volume that ensures that the prescribed dose is adequately delivered to the CTV in 90% of the population. It should be noted that in figure 5 most margins are not applied isotropically. The margin applied to the CTV is not only dependent on the source of the uncertainty, but also on surrounding organs at risk (OAR) and anatomical features.

During treatment planning, certain constraints are added to the known anatomy to ensure that the organ cannot receive a higher-than-safe dose that eventually can lead to



**Figure 5:** Illustration of the margin recipe according to the ICRU reports for motion management in photon therapy. PTV= planning target volume, ITV= internal target volume, CTV= clinical target volume and GTV= gross target volume.

toxicity. Even with these added constraints, the margins applied to the CTV more often than not included a large amount of healthy tissues limiting the total dose that can be delivered to the target volume.

Large margins lead to unnecessary dose to OAR and healthy tissues. The measurement and reduction of these margins have had much attention in radiotherapy research. The reduction of errors during the radiotherapy chain will lead to fewer uncertainties and consequently the reduction of margins. However, uncertainties will always be present and a certain margin is inevitable to ensure target coverage of the CTV [12].

The uncertainties or errors present in radiotherapy are classified as systematic errors and random errors. Systematic errors are errors that influence each treatment fraction in an identical way. Systematic errors have a similar magnitude and direction in all treatment fractions. As the systematic error is the same during all fractions it can cause a shift of the dose distribution in the direction of the systematic uncertainty. Random errors are uncertainties that differ from one fraction to another and do not have a systematic component and lead to the blurring of the dose distribution at the target. Sources of random errors can be patient or organ motion and differences in ambient

conditions. The concept of random errors and systematic errors is very important as these concepts are used to determine the magnitude of the margin for the patient from CTV to PTV.

## 2.1 CTV-PTV margin calculation

To calculate the margin, all systematic and random errors have to be considered. Systematic errors have a much larger effect on the dose distribution as it affects all fractions in a similar matter. For some patients, the shift of dose can lead to the CTV shifting out of the high dose region resulting in a strong effect on treatment. In contrast, random errors lead only to small decrease of dose at the edge of the high dose region (blurring of dose), which has only a moderate effect on patients. This has led to the development of a margin recipe, where systematic errors have a higher weighting than random errors:

$$A = 2.5\Sigma + 0.7\sigma \quad (2)$$

where A is the applied margin,  $\Sigma$  the systematic error and  $\sigma$  the random error [12]. Commonly, the margins are calculated for each specific treatment derived from a population of patients that received a similar treatment. From this population, systematic and random errors are calculated by determination of the error per patient per fraction. The systematic error is defined as the standard deviation of the error of the whole population while the random error is defined as the group mean of the standard deviation:

$$\Sigma = \sqrt{\frac{(\mu_1 - M)^2 + (\mu_2 - M)^2 + \dots + (\mu_p - M)^2}{n - 1}} \quad (3)$$

$$\sigma = \sqrt{\frac{(SD_1)^2 + (SD_2)^2 + \dots + (SD_p)^2}{n - 1}} \quad (4)$$

where  $\mu_p$  is the mean error per patient ( $p$ ), M is the mean error over the whole population,  $SD_p$  the standard deviation of the error per patient and n the population size.

This margin recipe is not the only margin recipe available, each recipe can have different interpretations considering the site that is treated, tumor control probabilities, the definition of errors and beam arrangements. The margin described in equation 2 is designed in such a way that it guarantees that for 90% of the population the CTV receives 95% of the prescribed dose [12].

## 2.2 Sources of uncertainty

To decrease the systematic and random errors in this margin recipe, and accordingly decrease the overall margin, the sources of errors have to be determined. Geometrical uncertainties cause these errors and there are four main sources: (a) Machine related

errors, (b) patient set-up variation (c) target tumor delineation errors, and (d) organ motion and deformation.

Each source attributes to a systematic error, random error or both. In a specific patient, these sources can be added linearly to compose the error and eventually the margin. For generalization to the whole population, the SD has to be calculated and the addition should be quadratically:

$$\Sigma_{total} = \sqrt{\Sigma_{machine}^2 + \Sigma_{set-up}^2 + \Sigma_{delineation}^2 + \Sigma_{organmotion}^2} \quad (5)$$

Machine-related geometrical errors caused for example by beam size deviations are minimized due to the development of accurate treatment delivery and well-regulated quality assurance. Machine related errors are thus relative small compared to the other sources of uncertainties and hence not a major issue [13].

The margins added for patient set-up errors are due to variations in the daily positioning of the patient on the treatment couch. Even though measurements are taken to improve patient setup verification (like CB-CT) variations in positioning still cause uncertainties that can result in an error during treatment. Setup errors have both a systematic error as well as a random component.

Target tumor delineation errors arise in the delineation process of the GTV. This includes the limitations on the resolution of the imaging modalities as well as observer variability (when observers are asked to delineate the target volume, differences between observers cause variations). An example of the observer variability is shown in figure 6, where 16 different observers delineated a pancreas tumor. This figure shows that the interpretation of observers can be very variable when the imaging quality is compromised or different guidelines for delineation are used. This delineation uncertainty is a systematic error, it will influence each treatment fraction in an identical way.

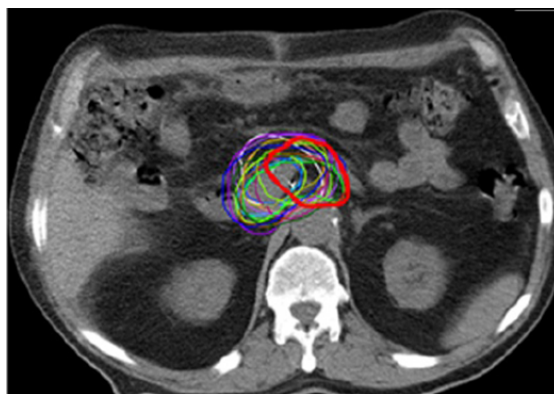


**Figure 6:** Inter observer variability, 16 different observers are asked to delineate a pancreatic tumor. Large differences are observed due to differences of image interpretation. Reprinted from [14].

The origin of organ motion and deformation will differ from day-to-day and can be

caused by variations in the bladder, stomach or rectum filling. While variations during a treatment day can be caused by cardiac or respiratory action. This causes the error of organ motion to be both systematic and random.

For reduction of the margins used in radiotherapy, the systematic and random errors should be minimized. Because systematic errors have a higher impact on the treatment and could lead to geometrical misses, systematic errors results in the need of larger margins than random errors.

The reduction of the systematic component could lead to a smaller margin and can be achieved by improving target volume delineation and organ motion determination.

The improvement of organ motion due to respiration can be achieved by adequate respiratory management while improving the image quality during pre-treatment imaging could lead to better target definition.

In this thesis, an imaging technique is developed to do exactly this: provide an excellent imaging modality with accurate motion management.

### 2.3 Respiratory motion management

The position of the tumor deviates due to respiratory motion. Tumor movement in the upper abdominal area can be as large as several centimeters due to respiratory motion. If this motion is not captured in an ITV it will result in a large systematic error.

The determination of the ITV for most abdominal structures is not straightforward. The deformation and motion of tumors and OAR are common due to non-rigidity of the structures and autonomous movement of bowels, stomach, heart, and the lungs.

Respiratory induced motion is hindered by the patient specific characteristics of the motion, inhibiting a population based CTV to PTV margin [15].

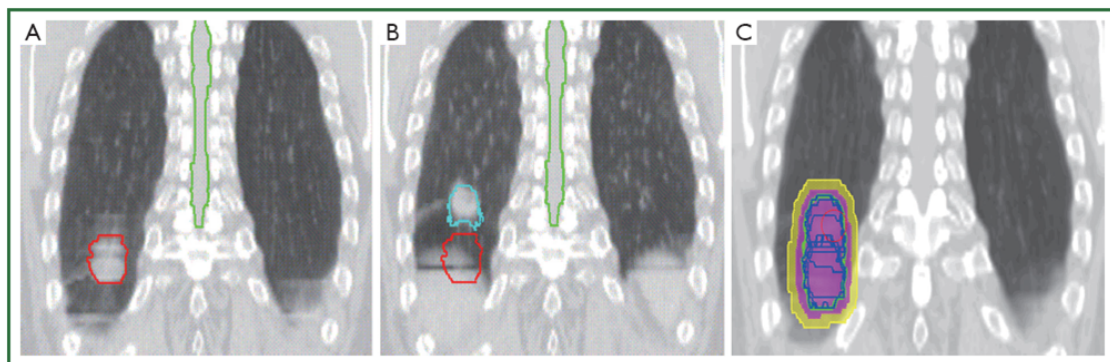


**Figure 7:** Determination of the ITV using 4D-CT volumes. The 4D-CT images are shown of end-inhalation (A) and begin-inhalation(B). All phases with the delineated tumors and margins are also shown (C). Figure reprinted from [16].

Advanced scanning methods like respiratory correlated CT or four dimensional-CT (4D-CT) are used to determine the ITV, reducing the systematic error [12]. In 2013, an estimated 60% of all the radiotherapy centers in the US use this technology to estimate

respiration-induced tumor motion. 4D-CT imaging, the acquisition of respiratory resolved images over time is used for 4D treatment planning and consequently for 4D treatment delivery.

The 4D-CT acquires typically volumetric images that are respiratory correlated. The number of volumetric images are set by the user. Each volume represents a respiratory state or respiratory phase. Figure 7A shows the delineated tumor in a volume at a certain respiratory state (end-inhalation). Figure 7B shows a volume in another respiratory state (begin-inhalation) showing the motion of the tumor in the SI direction. Figure 7C shows all delineated tumors from all respiratory states derived by the 4D-CT making it possible to determine an ITV.

### **2.3.1 4D-CT acquisition**

A 4D-CT is acquired by simultaneous acquisition of images and a respiratory signal. The respiratory signal is often generated by an external surrogate. The external surrogate can be: a reflective marker placed on the patients body surface that tracks abdominal displacement, spirometer with a thermocouple which measures temperature of the airflow or elastic belts that measure the pressure of the abdomen [17].

A 4D-CT acquisition method is illustrated in figure 8. At each couch position oversampling of the data ensures a sufficient number of CT slices over a certain width, so that there are enough images to achieve respiratory sorting with acceptable spatial accuracy. All the images obtained at each couch position are sorted into several respiratory bins based on the information obtained from the respiratory signal. Such a sorting procedure results in the classification of the over-sampled images into several respiratory-sorted image bins according to their respiratory phase. The respiratory phase is determined as the linear distribution of the respiratory cycle from phase 0% (begin-inhalation) up till phase 100% (end-exhalation) in equidistant bins, see figure 8.

The complete 4D-CT data set constitutes of a number of volumetric images or bins containing in each bin a whole volume at a certain respiratory state. The 4D-CT set contains a rich amount of information about pulmonary motion which is used for the benefit of radiation therapy. For example, a tumor may be tracked by defining an interesting region in a CT-image volume. The change of shape and position for this specific region can then be interactively tracked using the 4D-CT set.

### **2.3.2 4D-CT artefacts**

As mentioned above 4D-CT is a functionality that is used at the majority of the institutions and it aids in the improvement of radiotherapy treatment. Still, there are several limitations to this modality. As the same anatomy is imaged several times at each respiratory state, acquisition time increases leading to additional radiation dose to the patient. The total effective dose of a typical 4D-CT is 8 times the dose from a single conventional scan [19]. The dose is often affected by patient specific breathing patterns and oversampling parameters so for a 4D-CT scan the dose is in the range of 250-400 mGy in air. However, the major limitations of the 4D-CT are artifact creation due to

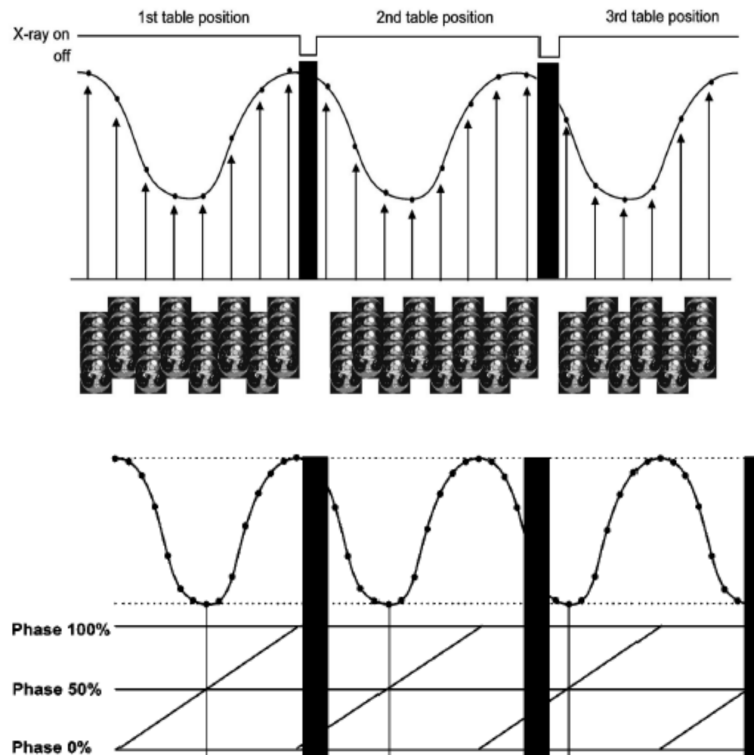


**Figure 8:** Representation of 4DCT acquisition. Simultaneous acquisition of CT-images together with a respiratory signal is performed (top). The respiratory signal is divided in a linear distribution of phases from 0 to 100% (bottom) and used to sort images according to their respiratory phase. Figure reprinted from [18].

irregular breathing.

Irregular breathing, temporal variations in breathing phase or amplitude cause mismatches between following phases or displacements between adjacent data segments (couch positions) in a 4D-CT scan. The consequence of these mismatches are artifacts in the 4D-CT dataset. These artifacts are primarily visible when reconstructing the axially acquired image slices into coronal or sagittal reconstructions. Figure 9 shows the four major classes of artifacts present in 4D-CT datasets.

Blurring occurs within one couch position when the organ motion exceeds the gantry rotation ( $\sim 500$  ms) of a scanned area. This is not related to respiratory motion as a respiratory cycle is typically 3-7 s.

In contrast, the other three artifact classes are contributed to respiratory motion variations and arise due to differences in respiratory states at the interface of two adjacent couch positions.

Yamamoto et al. [20] found that during a 4D-CT of 50 consecutive patients, 90% had at least one artifact due to respiratory variability with a mean magnitude of 11.6 mm

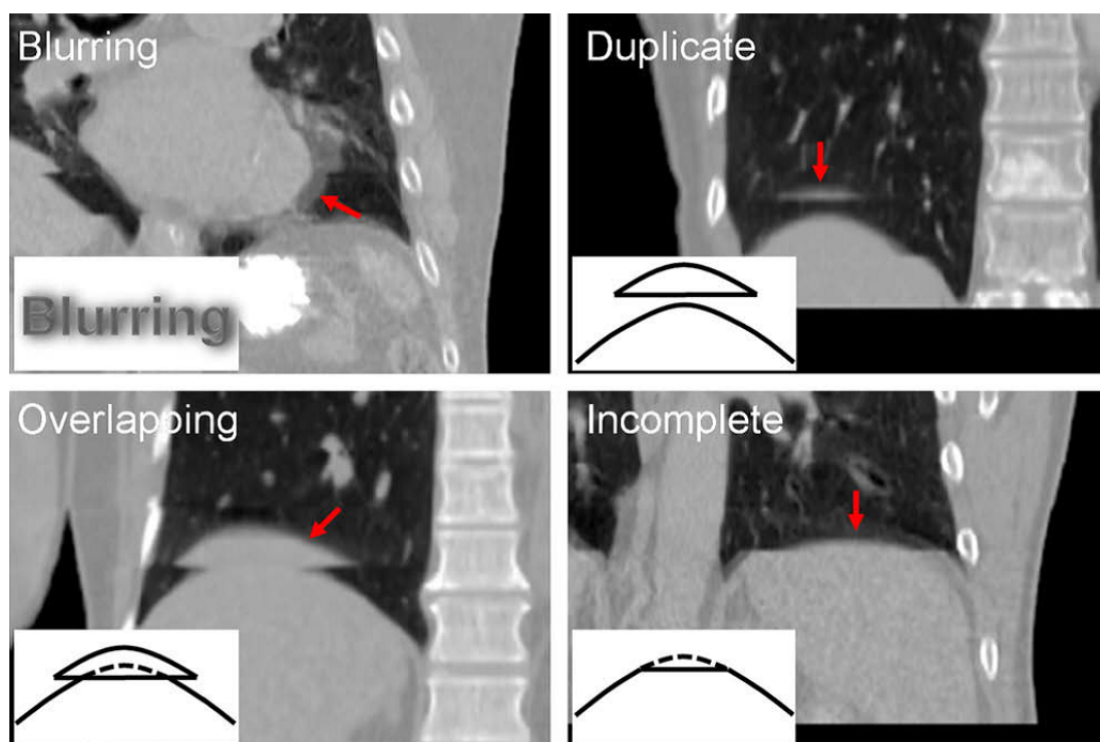


**Figure 9:** The four major classes of artifacts present in 4D-CT datasets. Duplication, overlapping and incomplete 4D-CT images arise breathing motion patterns, while Blurring occurs when motion exceeds the temporal resolution of the scan. Reprinted from [20].

(4.4-56.0 mm). This high frequency and magnitude shows the need for improvement of 4D-CT imaging.

For the improvement of respiratory correlated acquisition many methods have been proposed. These methods can also be divided into four categories: (1) Respiratory cycle control (2) respiration synchronized acquisition (3) improved post-processing and (4) improved sorting. The first two try to improve the acquisition of images while the latter two improve the eventual 4D data set from the original acquisition. Respiratory cycle control has the goal to improve the reproducibility of the patient's breathing cycle. The most common used method is to implement audiovisual feedback to guide the patient breathing during treatment or planning. The 4D-CT quality could improve by minimizing the mismatch between respiratory phases due to a predictable respiratory cycle. This method requires feedback equipment not available at every institution.

Respiration synchronized acquisition or gating, acquires CT data at predefined values (phase, displacement or velocity) of the respiratory cycle. Gating ensures that CT data from irregular breathing patterns are not acquired [21]. The advantage of gating is limited due to increased imaging times and consequently increased treatments time [22].

Improved post-processing methods have been proposed to create interpolated 4D-CT images at pre-defined respiratory states by deformable image registration. The best fitting CT image was chosen for 4D-CT reconstructions instead of the nearest available segment of the regular method [23]. This improved post-processing provides datasets with smoother transitions through a respiratory cycle. However, this method requires a well-validated deformable image registration technique.

Improved sorting strategies are also developed that does not depend on the linear distribution of the respiratory phase. Rather the displacement of the respiratory signal is used instead of the respiratory phase. This amplitude binning method resulted in better quality CT-images [24–26]. Irregular breathing can lead to gaps in the 4D-CT data set, which has to be considered when choosing amplitude binning.

Another possibility of improving the sorting of 4D-CT images is to choose for internal respiratory signal measurement instead of the widely used external surrogates for respiratory motion. The rationale for internal respiratory signal measurement is that it is better correlated to the respiration induced motion of the organs. It is found that 4D-CT data sets based on internal anatomical features like the diaphragm possess fewer artifacts than the images sorted by an external respiratory monitoring device [17].

The improvement of 4D-CT can be achieved using the above-described methods. Still, CT acquisition methods use radiation for image acquisition and the increased dose using 4D-CT is not desirable. For lung tumors, 4D-CT has proven to assist in accurate delineation of the tumor and the associated ITV [16]. However, this technique is poorly suited for abdominal areas due to the poor soft-tissue contrast of the CT and hence 4D-CT.

Other imaging modalities have to be chosen to track respiratory induced motion in the upper abdominal region. Magnetic resonance imaging (MRI) has developed parallel to CT into a powerful imaging modality. This modality obtains volumetric images, just like CT. However, it does not use ionizing radiation, has superior soft tissue contrast and the potential for tumor to tissue contrast. These advantages can be combined with the improvements of respiratory correlated images described in this section to develop an accurate respiratory correlated MR method.

### **3 Magnetic Resonance Imaging**

The MRI is a very versatile non-invasive imaging technique with many applications in medicine. In a radiotherapy context, MRI has been integrated in the preparation for treatment mainly due to its superior soft-tissue contrast. Next to the improved contrast, MRI does not expose the patient to ionizing radiation, offers the possibility to perform functional imaging providing biochemical information, and has the possibility of high resolution imaging unrestricted to a certain imaging plane. MRI images do not directly obtain information on the electron density of structures needed for treatment planning. Therefore, MRI is often integrated in the radiotherapy workflow in combination with CT.

The development of a respiratory motion management technique analogous to 4D-CT could benefit from the advantages of MRI and could aid in the motion management of abdominal tumors. This chapter covers the aspects of data acquisition for MR image acquisition and reconstruction. The understanding of concepts like the spin-echo, image contrast, signal-to-noise ratio, resolution and acquisition time all play an important role in the development of a scanning sequence. This sequence is needed for the development of a respiratory correlated magnetic resonance data set with abdominal structure contrast.

### 3.1 Basic MRI physics

The MRI uses a strong magnetic field to probe subtle changes in the magnetism of a nucleus. Not all nuclei possess magnetic properties but the nuclei of protons do. The MRI is based on the sensitivity to the presence and the properties of protons in tissues and creates images accordingly to differences in proton properties.

#### 3.1.1 Spins in a magnetic field

The nucleus of a hydrogen atom, a single positively charged proton, rotates around its own axis. The proton is thus a continuously rotating positive charge. This moving charge induces a current and is therefore associated with a magnetic field. This means that each proton generates its own tiny magnetic field or more precisely has its own magnetic moment. It is this magnetic moment that interacts with the large magnetic field of the scanner. When this proton is placed inside a strong external magnetic field it experiences a torque that tries to align the proton with the magnetic field. The spin cannot align itself completely to the magnetic field and this causes it to precess around the direction of the field. The precessional frequency of the protons is found to be proportional to the applied external magnetic field (from now on:  $B_0$ ) given by the Larmor equation:

$$\omega_0 = \gamma B_0 \quad (6)$$

where  $\gamma$  is the gyromagnetic ratio and  $\omega$  the Larmor frequency. A single spin in a magnetic field can exist in two states. One state, known as the spin-up state is parallel aligned to the magnetic field. The other state is aligned antiparallel to the field and is commonly known as the spin-down state. Both states are energetically favorable and thus stable, however, the spin-up state requires slightly less energy. This state is favored resulting in slightly more (4 out of  $10^6$ ) spins parallel to the magnetic field. The ratio of spin-up and spin-down states is dependent on the strength of  $B_0$  and inversely proportional to the temperature.

A group of protons in equilibrium precess around the magnetic field with each single spin in one of the two states. In equilibrium no phase coherence is present, so each magnetic moment is evenly distributed around the precessing trajectory as illustrated in figure 10a. Each vector represents a spin (or group of protons) precessing at the Larmor frequency at a certain location (phase) of the precessing trajectory (circle). The sum of all spins is called the net magnetization  $M_0$ , which is aligned exactly with

the main field  $B_0$ . The magnitude of the net magnetization is dependent on the ratio of spin-up and spin-down and this macroscopic quantity is measured.

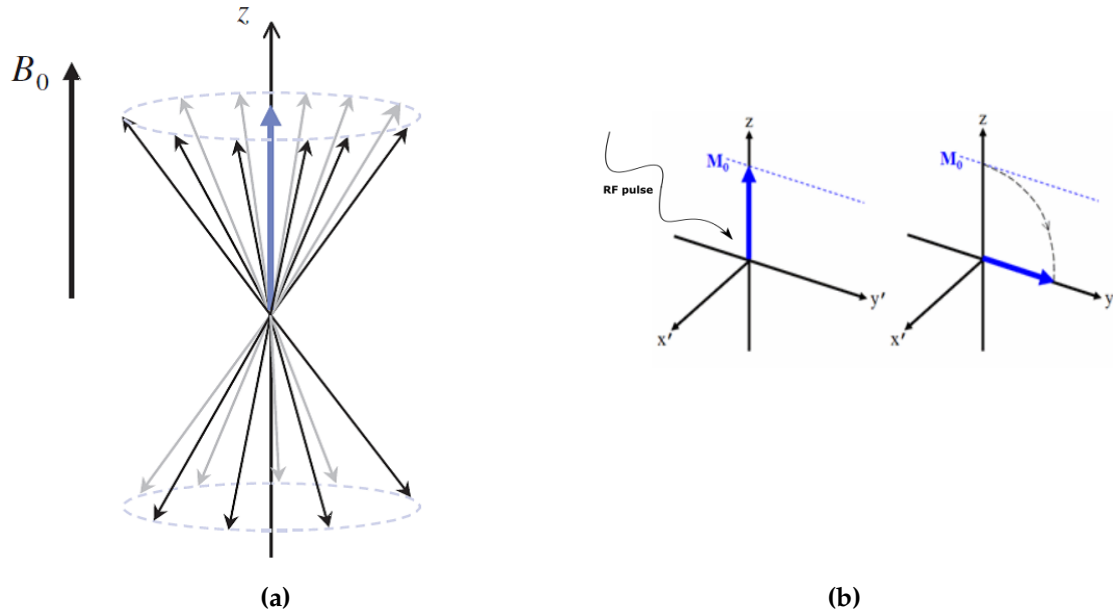


**Figure 10:** (a) All spin state (spin-up and spin-down) in an external magnetic field ( $B_0$ ). The average calculated from the ratio of spin-up and spin-down produce the net magnetization  $M_0$  (blue arrow). Figure reprinted from [27]. (b) The RF-excitation pulse flips  $M_0$  90° into the transverse plane, making it possible to measure  $M_0$  in the transverse plane ( $y$ ).

### 3.1.2 Measuring the spin-echo

The net magnetization induced by the differences of the occupation of states can be measured. However, when the spins are aligned to the magnetic field the magnitude of  $M_0$  is very small ( $\mu\text{T}$ ) compared to  $B_0$  ( $\sim 3\text{T}$ ). To distinguish the net magnetization from the external field, detector coils that measure only the magnetization perpendicular to the magnetic field are used. To measure the net magnetization in the so-called transverse plane, the spins are flipped 90° by a radio frequency (RF) pulse, see figure 10b. Only when the frequency of the RF pulse matches the Larmor frequency, the so-called resonance condition, the spins can be flipped into the transverse plane. If  $M_0$  ends exactly in the transverse plane, then the RF pulse is called a 90° pulse or excitation pulse.

Another effect on spins induced by the RF pulse is putting the spins into phase coherence. This means that the spins mostly are at the same position on the precessing trajectory. The net magnetization in the transverse plane is largest when all spins are in phase and this is the case directly after the excitation pulse. This large magnetization

induces a voltage in a coil which can be measured. This coil sees an oscillating magnetic field which induces a voltage varying at the Larmor frequency. However, the signal decays rapidly (ms) because the spins dephase with respect to each other.

It is however not the  $M_0$  directly after the excitation pulse that is measured but an echo created by a sequence of RF pulses. These echoes are brief moments in time where the spins are all in phase creating a large  $M_0$ . In MRI, two methods are used to create echoes: gradient echoes and spin echoes. During my research, I used only spin echoes so we will focus on this type of echo creation only.

To measure the spin-echo two consecutive RF-pulses are applied (figure 11). After the excitation pulse, the spins are left to dephase naturally for a certain time. Then an  $180^\circ$  pulse is applied which flips all the spins  $180^\circ$  on a certain axis (in this case the 'y' axis), see figure 11d. This pulse causes the dephasing spins to be reversed in phase. After this pulse, all the spins continue to change phase like before, however because the phase was reversed the spins start to become more phase coherent (figure 11e). After exactly the time in between the excitation pulse and the  $180^\circ$  pulse all spins are in phase again.

## 3.2 Image acquisition and reconstruction

With the use of the above-described spin echo, protons in tissues can be probed. In the following section, it is described how to differentiate between different tissue types and how an MRI image is created.

### 3.2.1 Relaxation time

The most important properties that are exploited by the MRI-scanner are the relaxation times of protons in different molecules. There are two main features of relaxation: (1) the realignment of the spins along  $B_0$  as the excited spins lose energy and (2) the dephasing of spins after their phase coherency following excitation. The two characteristic relaxation times are denoted  $T_1$  and the earlier mentioned  $T_2$ . Both relaxation times are tissue dependent and the differences in relaxation times arise from the amount of protons present in the tissue, the bounded state of the proton and the possibility of interactions between protons. The most important message is that different structures have different relaxation times and these differences cause the contrast in the image.

In general one of the two relaxation features dominates the contrast in the image and this is dependent on the sequence parameters. Figure 12 shows a  $T_1$ -weighted image and a  $T_2$ -weighted image of the abdomen. Commonly  $T_1$ -weighted images are used for anatomical purposes and  $T_2$ -weighted images for pathology. MRI allows us to produce a wide range of contrast by choosing different techniques and sequence parameters. The most important parameters that determine if an image is  $T_1$ - or  $T_2$ -weighted is the repetition time (TR) and the echo time (TE). The TR is the time between each consecutive excitation pulse and TE is the time between each excitation pulse and the echo (see figure 11a).

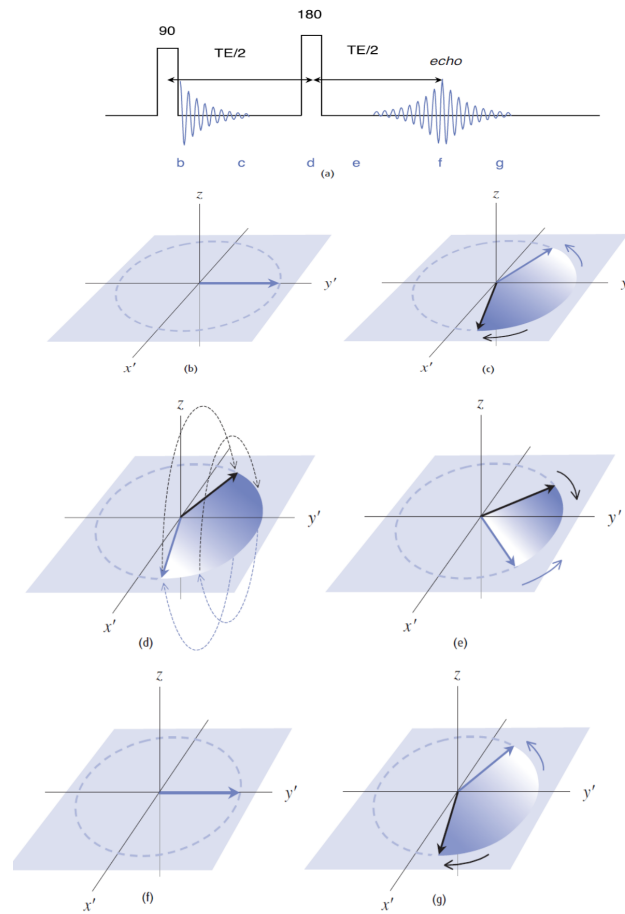


**Figure 11:** A spin echo sequence is displayed (a). The coherent spins show large transverse magnetization after the excitation pulse(b), the spins then dephase naturally(c) until the 180° pulse(d). The reversed spins continue to change phase (e) until they are coherent again and form an echo(f). After the echo the spins lose coherence again (g). Figure reprinted from [27].

On  $T_2$ -weighted images, fluids have the highest intensity and water and fat based tissues are mid gray. This makes it often very suitable for distinguishing pathology because abnormal fluids are bright against the darker 'normal' tissues (see figure 12b). In the abdominal region, the contrast between all soft tissue organs has shown to be the best for  $T_2$ -weighted images [29]. Also the tumor to tissue contrast in  $T_2$ -weighted images, for treatment purposes a very important parameter, has shown to be very good in liver tumors [30].

To achieve images with  $T_2$ -weighted contrast TR and TE have to be large compared to  $T_1$ -weighted images, which increases scan time. The versatile MRI modality makes it possible to acquire a wide range of images each with different optimization parameters.

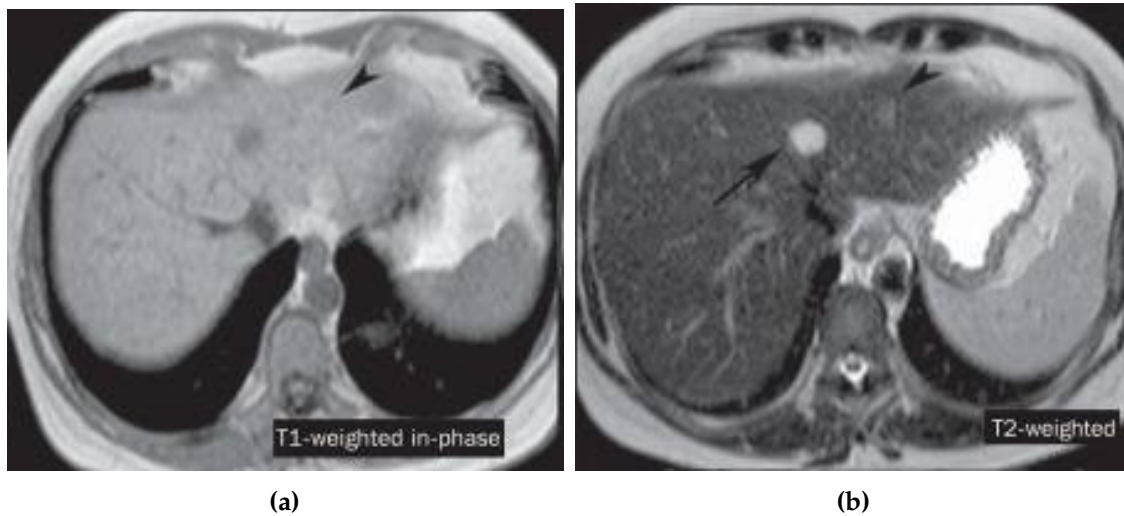


**Figure 12:**  $T_1$  weighted (a) and  $T_2$  weighted images of the abdomen. The arrows indicate the higher contrast of lesions in the liver with  $T_2$ -weighted sequences. Reprinted from [28].

The spin echo relies heavily on the reversal of spin phase, it has the advantage that it only depends on the  $T_2$  relaxation time and is not susceptible to subtle changes in the magnetic field induced by tissues with magnetic properties (inhomogeneities). The spin echo is used in a sequence to acquire an image.

### 3.2.2 The spin echo sequence

An MRI image consists of a matrix consisting of gray scale pixels. The gray scale image is reconstructed from a raw data matrix known as k-space. The k-space matrix is a matrix filled with all the information acquired during image acquisition. In the most simple spin echo sequence, a row in k-space is filled with every TR. Each time the sequence is repeated a full line of data is acquired. Then acquisition parameters are changed and another row is filled with new data. The size of the image is directly related to the size of k-space and the acquisition process continues until all rows are filled and the image is reconstructed using a Fourier transform.

To differentiate each pixel in the resulting image, the intensity variations and the location of the voxel it represents should be determined. Different gradients are used to determine the MR signal positions in space. A gradient, a controlled variation of the static  $B_0$  field can be used to locally increase or decrease the resonance frequency of the spins. Faster or slower precession is detected in the MR-signal as higher or lower frequencies and in this way can be used to distinguish between protons in space.

To image the required slice from the patient a slice selective gradient and excitation pulse is applied. Figure 13 shows a standard spin echo sequence where the slice selective gradient ( $G_{ss}$  and the RF pulse are displayed). The gradient changes the Larmor

frequency of all the protons and the RF pulse contains a narrow range of RF frequencies centered around a chosen Larmor frequency at the slice of interest. This process will cause only the protons in the bandwidth of the RF pulse to resonate and this selects the correct slice for data acquisition. The operator can manipulate the position, thickness and orientation of the slice by adjusting the  $G_{ss}$  or the RF pulse. The slice location can be changed by the operator by changing the chosen frequency of the RF pulse. The thickness of the slice can be altered by either changing the RF bandwidth or the gradient slope. Decreasing the bandwidth with the same gradient slope would result in thinner slices while decreasing the gradient slope with the same RF pulse bandwidth increases the slice thickness. The orientation of the slice can be tailored by choosing physically other gradient directions.

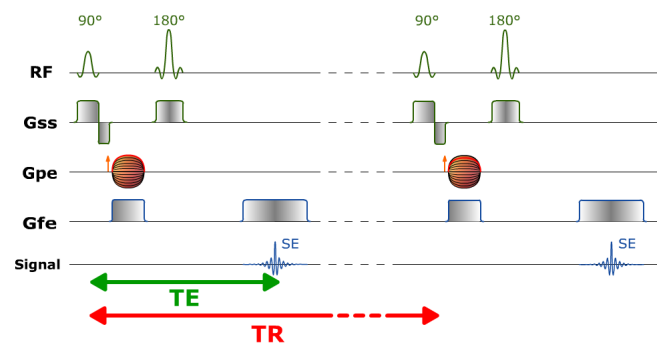


**Figure 13:** Diagram of spin-echo sequence showing the RF excitation pulse, the slice selection gradient  $G_{ss}$ , the phase encoding gradient  $G_{pe}$  and the frequency encode gradient  $G_{fe}$ . Figure reprinted from [31].

After selection of the slice of interest using  $G_{ss}$ , the phase encoding gradient  $G_{pe}$  and frequency encoding gradient  $G_{fe}$  are applied to acquire the data of the 2D-slice. The phase encoding gradient is represented as a series of parallel lines in figure 13. This is because at each TR a different phase encoding gradient is applied until all necessary data is obtained.

The phase encoding gradient applies a gradient in a certain direction which will speed up or slow down protons according to their position in the gradient. After a certain time the gradient is turned off and the protons will revert to their original speeds. However, because some protons were precessing faster than others, certain positions in the slice are not in phase anymore. The protons are said to be phase encoded. The phase encoding step is used to acquire signals from the selected slice to probe differences in response to variation in phase encoding amplitudes. Each response to a different phase encoding amplitude is called a spatial frequency and determine the grayscale values in the image.

One phase encoding direction (in a 2D-plane) only probes one direction in the slice. The other direction in the slice must also be obtained to acquire a 2D image. It could be possible to apply another phase encoding gradient and apply the same procedure again. However, this would result in a time-consuming procedure as each

point in k-space would require one whole TR. The solution is shown as the last line in figure 13 and is called the frequency encode gradient  $G_{fe}$ . This gradient is applied continuously and by changing the time positions that the MR signal is measured the spatial frequencies can be measured. At each measuring point, the MR signal is measured with a different amount of phase change due to the continuously applied gradient. Each data point reflects the encoding in the precessing phase and thus corresponds to a spatial frequency. This process is analogous to the phase encoding direction. However, the whole line of k-space can be acquired during the time of one TR because of the continuous acquisition of all spatial frequencies when the gradient is on.

Because the whole line of frequency encoding is acquired during one TR, one could argue why phase encoding is needed. The reason for this is that frequency encoding is a scalar parameter. The application of the frequency-encoding gradient in two directions would make it impossible to distinguish between the two. This makes it important to combine phase encoding and frequency encoding in the two orthogonal directions of the slice to collect all MR-signals and derive their positions.

From the filled k-space data an image can be reconstructed by extracting from all the spatial frequency data the intensity of the signal and the position. This information is incorporated in the phase encoding and frequency encoding steps and extracted by reconstructing the image using the Fourier transform. The size of the area covered by the matrix created from the phase encoding and frequency encoding steps is called the field of view (FOV).

### 3.3 Spin echo optimization

The spin-echo sequence could result in  $T_2$ -weighted images if the TR and TE are chosen correctly.  $T_2$ -weighted contrast is needed to achieve high soft tissue contrast in the abdomen. For high quality 4D-MRI, not only the contrast is important, also additional parameters like the spatial resolution, temporal resolution, and signal-to-noise-ratio (SNR) have to be considered.

To distinguish organs in the abdomen, the resolution of the reconstructed image should be adequate with a resolution of at least 2 mm. However, to avoid respiratory motion induced artifacts in the acquisition of images, the temporal resolution should be adequate. Because a respiratory cycle is 3-6 seconds, a frame rate of more than 1 frame per second (1 Hz) is an appropriate temporal resolution for 4D-MRI. Finally, the SNR should be considered to avoid noisy images. The SNR, temporal resolution and spatial resolution are all interconnected and changing one would definitely influence one of the others. Concessions have to be made to acquire an image suitable for 4D-MRI.

#### Resolution and SNR

In MR not only the in-plane resolution should be considered but also the through plane resolution or slice width is an important parameter. Together with the resolution, the SNR should also suffice. The SNR is the ratio of the signal intensity and the background

noise.

High MR signals arise from the amount of signal in the imaging plane (FOV) divided amongst the voxels that make up the image. The intensity of the signal is thus directly related to the voxel size, larger voxels yield higher signal.

Noise arises from random fluctuations in electrical currents. These currents exist in all electrical conductors including the MR coils but also in human tissues like the nerves. These currents generate fluctuating magnetic fields which induce a noise voltage in the coils, which is a random component in the image.

The trade-off between resolution and SNR is one that is quite complicated, also because many user-controllable scanner parameters affect them. The most common consideration of MRI users is to reduce the slice width to be small enough to visualize small anatomical detail. However, if the slice width is chosen too small the lowered signal to noise ratio could result in a fuzzy bad quality image, where boundaries are hard to distinguish and the contrast is not sharp. The same argument holds for in-plane changes of the voxel size. However, pixel dimensions (typically  $1 \times 1 \text{ mm}^2$ ) of the image are often chosen relative small to the slice width (typically 5 mm) to achieve high in-plane resolution.

### **3D acquisition**

Very thin slices are advantageous because when a whole volume is studied, a multiplanar reconstruction can be used. These reconstructions view the acquired volume from different viewing planes than the original acquired plane. For example, a transverse (axial) reconstruction is created from images that are acquired with a frontal (coronal) view. Very thin slices will allow for isotropic imaging, where the reconstruction from other planes has the same image quality of the original imaging plane. To acquire very high resolution (a very thin slice) with sufficient SNR the transition of a 2D-acquisition to a 3D-acquisition is a possibility.

To achieve 3D acquisition, an extra phase encoding gradient is added to a 2D sequence to encode the third dimension. This will result in excitation of the whole volume at each TR and consequently, a 3D k-space matrix will be filled. With the use of a 3D-Fourier transform, the whole volume can be reconstructed into a 3D volume consisting of very thin 2D slices.

The advantage of this method is that the signal comes from the whole volume at each TR instead of a selected slice, which will improve the SNR. Moreover, because a 3D-volume is acquired the spatial resolution is excellent with the possibility of high-quality multiplanar views. This in contrast to the acquisition of 2D slices, where the lack of resolution in the width of the slice could cause artifacts in the multiplanar reconstruction.

As an extra phase encoding gradient is added and the whole 3D matrix has to be filled, the acquisition time of a 3D acquisition is long. This is the reason that 2D acquisition methods are still used as they can achieve a higher temporal resolution. To track the respiratory motion of organs and tumors, a very fast sequence is required.

With the currently available scan protocols, this will omit 3D acquisition as a suitable candidate. The normal spin echo sequence, which gives  $T_2$ -weighting with long TE and TR is often not fast enough to capture respiratory motion. The need for a fast sequence, with  $T_2$ -weighting, good SNR, and sufficient spatial resolution has led to the turbo spin echo (TSE) sequence.

### 3.3.1 The turbo spin echo sequence

Spin echo type of sequences can be acquired with substantial time saving by collecting more than one line of k-space per excitation pulse (TR). This is achieved by forming a train of echoes formed by multiple refocusing pulses, see figure 14. The sequence in figure 14 is the single-shot TSE (SS-TSE), a single excitation pulse is used to acquire a whole image. The evenly spaced refocusing pulses of  $180^\circ$  form an echo-train and these echoes are used to fill each line of k-space. The dephasing gradients are applied after each echo to ensure different phase encoding for the next echo. The TR for SS-TSE is in practice infinite and this sequence is often used for multiple slice acquisitions. Where each whole slice is acquired before moving on to the next slice.

Each echo in the consecutive echo train only has sufficient  $T_2$ -weighting if and only if the signal is high enough and not diminished by  $T_2$  decay. However, it is difficult to fill the whole k-space before the signal is decayed due to relaxation. Therefore, it is important to apply techniques that can reconstruct acceptable images with compromised k-space filling.

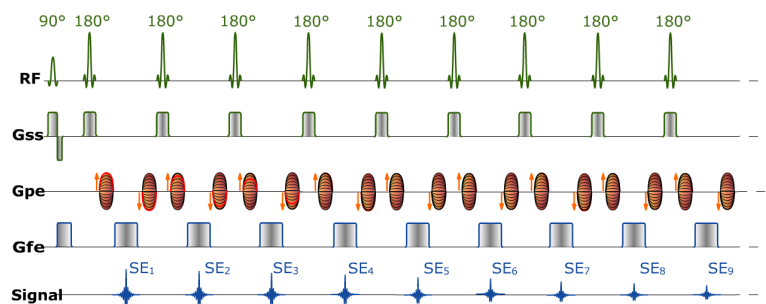


**Figure 14:** Single shot turbo spin echo (SS-TSE) sequence. Only one excitation is used to acquire the entire k-space. After each echo a RF pulse of  $180^\circ$  is applied to refocus the spins. As there is no time for the spins to dephase, dephasing gradients are added to the phase encoding step after each echo. Figure reprinted from [31].

The most common method to overcome undersampled data is the Half Fourier technique. This technique only needs slightly more than half of the k-space lines to reconstruct the image. The missing part of the data is estimated by applying conjugate synthesis, which exploits the symmetric properties of k-space. This technique combined with the SS-TSE sequence makes it feasible to obtain 2D-images with a frame rate higher than 1 Hz.

As always with MRI, there are quite some compromises involved with this sequence. First of all the large amount of RF pulses delivered to the patient can deposit large amounts of energy leading to tissue heating with possible physiological effects like changes in cardiac output. To limit the maximum energy deposited in the tissues of the patient the specific absorption rate (SAR) is determined and limited. The SAR defined as the total power (W) per kilogram of tissue could limit the amount of slices acquired during acquisition. Another major consequence is that the spatial resolution depends on the  $T_2$  of the tissues contributing to the signal. When a single shot is used with in principle an infinite echo-train length the spatial resolution will be decreased because it is difficult to distinguish between two small structures with fast  $T_2$  relaxation. This will lead to blurring [32,33].

Another property of TSE sequences is that fat signals are very bright. This can be advantageous for our purpose because in the abdomen, fat can outline all of the organs and the bowel improving contrast. However, very bright signals can obscure subtle intensity differences or conceal pathology. The last problem arises because of the multiple slice acquisition. As the images are acquired with a very high temporal resolution there can occur cross-talk between adjacent slices. The reason that crosstalk occurs is that slice selecting gradients have often a curved profile due to inhomogeneities in the  $B_0$  field due to imperfect gradients and distortions due to patient. Therefore, tissues in the overlapping region are excited by two slice selecting gradients. And because the temporal resolution is so high it does not have the time to relax so its intensity is influenced. The solution for cross talk is to include a gap between two adjacent slices. However, this will influence the spatial resolution. If a contiguous slice is preferred an interleaved acquisition method is a solution. This acquisition does not acquire images sequentially but in an 'interleaved' way. For example, a volume consisting of 11 slice position would not acquire the image from 1 ascending to 11 but in the order: 1,4,7,10,2,5,8,11,3,6,9. This gives the adjacent slices time for relaxation and prevents cross-talk.

### **3.3.2 Respiratory motion in MRI**

The fast SS-TSE sequence makes it possible to obtain good quality images with high temporal resolution making it feasible to capture anatomy without motion induced blurring. A major source of motion induced artifacts is motion induced by respiration. This respiratory motion which is often avoided by designing scanning protocols of under 25 seconds, making it feasible to acquire a scan during breath hold. Breath hold is not always suitable because the health of the patient can make it hard to comply to the breath hold. Also, it is challenging to repeat each consecutive breath hold in exactly the same way, which makes repeatability an issue. Moreover, autonomous motion like bowel movement can still cause blurring of target organs. Finally, even during a single breath hold the anatomy is moving which causes artifacts in the image.

If a breath hold is not suitable there are two ways to reduce artifacts due to respiratory motion: respiratory gating, and respiratory reordering. Like in 4D-CT,

respiratory motion tracking is needed. This can be accomplished using either external or internal monitoring devices. The external monitoring devices are similar to that of 4D-CT.

Navigator echoes, an internal monitoring device, do not use external devices for respiratory motion tracking but use a rapid 1D imaging method to map the position of the diaphragm. A 15-30 mm thick column is defined across the right diaphragm as shown in figure 15a. This column is acquired using a standard sequence without the use of phase encoding, the column is frequency encoded along the superior-inferior (SI) direction. The result is a line of voxels which have a strong contrast between the dark lung and the brighter liver. When a series of linear navigators is acquired while the patient is breathing, the changing position of the diaphragm over time can be visualized, as shown in figure 15b.

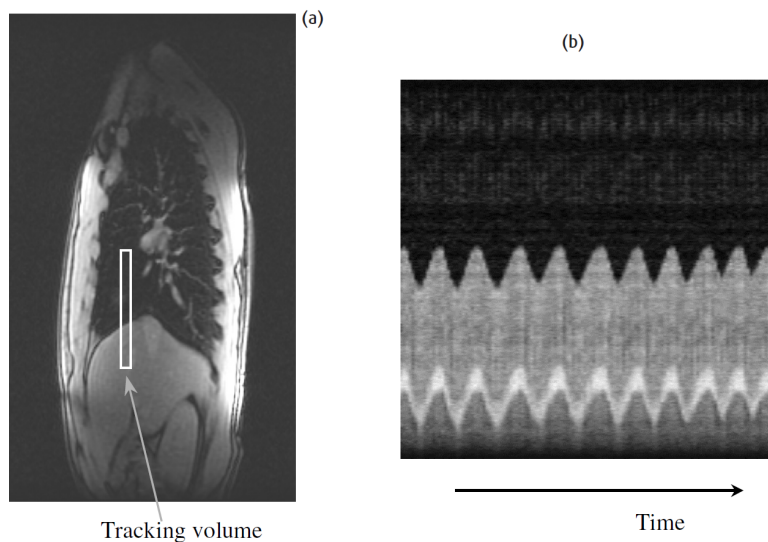


**Figure 15:** (a) The navigator echo excites a column that is tracked for respiratory motion monitoring. (b) The navigator signal is frequency encoded in one direction and tracked over time. Figure reprinted from [27].

Respiratory gating or prospective gating uses the respiratory waveform to start the imaging sequence at a predefined place in a breathing cycle, similar to gating of 4D-CT. This result is that each data line is acquired when the chest wall is approximately in the same position, so no motion artifacts are present in the resulting image. Because acquisition of the data only happens at predefined positions the downside of respiratory triggering is that acquisition can take very long. Especially when a patient has a very irregular breathing pattern the predefined triggering condition will not be reached, leading to extra scan time. Moreover, because the sequence is now dependent on the triggering of acquisition, the TR is not a controllable parameter anymore but dependent on the number of respiratory cycles during acquisition [27].

Respiratory reordering or retrospective sorting acquires the respiratory signal passively during acquisition. This respiratory signal together with the acquired images is then sorted offline after data acquisition in new images or image sets. This sorting can be applied to the already reconstructed images but can also be used to sort the k-space data according to the diaphragm position extracted from the respiratory signal.

My research has set the goal to develop such a sorting method using MRI together with a navigator to make it possible to retrieve an 4D-MRI image set that is respiratory correlated.

## Part II

# Research

## 1 Introduction

MRI has been used for radiotherapy treatment since the 1980s and its use is still evolving with new imaging techniques, opening new diagnostic and therapeutic scenarios. Due to its superior soft-tissue contrast it has been integrated into the radiotherapy chain through image co-registration complementing the use of CT.

The established CT modality and respiration management technique 4D-CT lacks tissue contrast in the abdomen. The small confidence in accurate position determination of organs and tumor have lead to large margins during radiotherapy treatment preparation. This limits dose to target volumes and have limited treatment outcome of abdominal tumors.

Abdominal lesions are especially difficult to treat due to their mobility. The implementation of MRI as high quality imaging modality together with a motion management technique could aid in the improvement of the treatment outcome of mobile abdominal lesions like pancreatic tumors.

### **Pancreatic tumors**

Pancreatic tumors have a bad prognosis. The 5-year survival rate is less than 6% [34]. A reason for this low survival rate is the difficulty to accurately deliver and conformally plan radiation therapy to the pancreatic tumor. The dose delivered to the tumor is inhibited by large margins applied to these abdominal structures. These large margins arise from the compromised visibility of this organ on CT, the position of this organ close to sensitive organs like the stomach and duodenum, and deformation of this organ due to (semi-)autonomous motion like bowel movements and respiration. The potential of good imaging of the organ combined with a sophisticated respiratory motion management technique could decrease the applied margins to the CTV. The systematic error could be reduced by reducing the delineation uncertainty and the component of the respiratory induced error could be diminished by accurately determining respiratory-induced motion. The decrease in the margins would allow the increase of the prescribed dose while limiting the dose to the sensitive organs. This could lead to a better control of the tumor while the toxicity of the treatment is minimized, potentially improving the quality of life for the patient.

### **Respiratory management**

Currently, a method to account for respiratory motion is four-dimensional imaging and planning [35]. In 4D-CT, the acquisition of the data set relies mainly on phase binning [24]. Artifacts present in the 4D-CT data set inhibit exact determination of the ITV and this is mainly contributed to irregular breathing and patient motion. The application of 4D-CT in abdominal tumors has however been limited. The inherently

low soft tissue contrast and low tumor to tissue contrast of CT images have hindered the accurate delineation of abdominal structures. In addition, long 4D-CT acquisition times increase the dose to the patient.

To overcome these limitations, several techniques based on four-dimensional magnetic resonance imaging (4D-MRI) have been proposed as an alternative for 4D-CT [36–40]. The potential for improved soft-tissue contrast combined with the versatility of the imaging modality makes 4D-MRI a suitable candidate for a respiratory management technique with high delineation accuracy.

The first thorough description of a 4D-MRI was performed by von Siebenthal et al [36]. A tailor made 2D navigator acquisitions of liver structures was interleaved with dynamic 2D images. The navigator was used to determine the respiratory state of the liver by looking at anatomical changes of liver structures. This navigator was used to match each 2D slice to a respiratory state according to the navigator. The so-called retrospective method showed high volume consistency and can be used to study respiratory induced organ motion. However, the feasibility of clinical implementation was hindered by acquisition times of tens of minutes, complex liver state determination and tailored sequence programming.

The concept of retrospective sorting of 2D images after acquisition (so called image-based sorting) was further developed by several groups. Different respiratory surrogates like external monitoring devices [39] and image-based body area [38] were investigated. These methods are feasible for clinical implementation as they use available protocols without sequence modification. The balanced steady-state free precession (b-SSFP) sequence used in these methods show high temporal resolution (>3 frames per seconds). Still, the sequence is very artifact sensitive, has reduced  $T_2$  contrast and showed reduced signal to noise ratio to commonly used  $T_2$ -weighted images [41].

Prospective sorting, in contrast to retrospective sorting, acquires images at predefined conditions in the respiratory cycle [42,43]. This method analogous to the gating in CT described in part I should improve 2D-acquisition efficiency or obtain 3D-volumetric images from a certain respiratory state. However, prospective sorting suffers from degraded 2D-acquisition efficiencies due to inconsistent breathing patterns, e.g. prolonged acquisition times. Also, real-time 3D acquisition faces challenges acquiring sufficient temporal resolution to capture a whole anatomy in less than one second, resulting in degraded resolution.

To improve the temporal resolution for 3D-image acquisition several techniques based on respiratory sorting of k-space instead of image-based sorting was developed [37,44–46]. K-space sorting relies on 3D acquired MR data where k-space lines instead of reconstructed images are assigned to a respiratory state. The 4D acquisition is completed in a fixed scan time and provides both high temporal and high spatial resolution [46]. Eventually, images are reconstructed from the raw acquisition data into respiratory sorted volumes. The filling of all available k-space lines could rise problems as beforehand it is not directly evident if all k-space lines are filled. The handling

of under sampled data can be solved by signal processing tools like partial Fourier Techniques, sensitivity encoding (SENSE) and compressed sensing. Although these techniques sound promising, it suffers from blurred and noisy images [44], inherent compromised abdominal structure contrast, band artifact sensitivity. Furthermore, as it is not yet commercially available either offline reconstruction tools or custom scanner software packages are required [37].

### **Purpose**

Abdominal tumor target delineation and treatment outcome could benefit from an accurate 4D-MRI method with high abdominal structure contrast.  $T_2$ -weighted spin echo sequences often show good tumor contrast in liver patients [30] and in other abdominal structures like the pancreas, the soft tissue contrast is excellent [29]. 4D-MRI with  $T_2$  weighted contrast is therefore desirable. Still, a low temporal resolution has hindered the implementation of this sequence into respiratory management. The development of single-shot turbo spin-echo (SS-TSE) has improved the temporal resolution making it a proper choice for 4D imaging.

The goal of our study is to develop an accurate 4D-MRI method with abdominal contrast ( $T_2$ -weighted) that can be practically implemented in the clinical workflow within a clinical relevant acquisition time of under 10 minutes. Together with high resolution (<2mm) images, it should result in high quality 4D-MRI data sets. A retrospective 4D-MRI technique using a navigator as respiratory motion tracker is proposed. This study explores the feasibility of a 4D-MRI method using two different type of respiratory state assignment methods: amplitude and phase binning. These two methods are compared and evaluated on robustness against irregular breathing, accuracy, and acquisition time.

The accuracy and feasibility of a 4D-MRI method using SS-TSE and a navigator are explored and validated on 12 volunteers.

## 2 Methods

### 2.1 Image acquisition

The acquisition of T2-weighted images was achieved using a 3.0 T MRI scanner (Ingenia 3.0T, Philips Healthcare, Best, The Netherlands). The SS-TSE sequence with a sequential acquisition in interleaved sub-mode was optimized for abdominal contrast and planning was focused on the pancreas. The choice of the planned structure could be extended to other abdominal organs by tailoring the sequence parameters. Image acquisition was performed in the coronal plan. The coronal plane separates the body from front to back, see figure 16. Coronal acquisition allowed for efficient anatomical coverage of the pancreas. Next to efficient volume coverage the coronal acquisition allowed for analysis of the diaphragm. During image acquisition the diaphragm is captured in the image together with the pancreas.

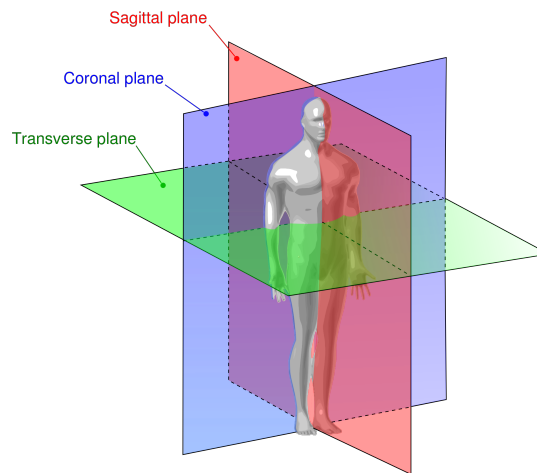


**Figure 16:** The clinically most used anatomical planes showing the coronal, sagittal and axial (transverse) plane.

Image acquisition was performed on 12 volunteers (8 female, mean age 28 years) with image parameters:  $1.3 \times 1.6 \text{ mm}^2$  in-plane resolution, slice thickness 5 mm, FOV:  $400 \times 200$  (SI  $\times$  RL)  $\text{mm}^2$ , TR 551 ms and TE 50 ms. The voxel size was chosen such that a high in-plane resolution is achieved while the SNR is kept adequate by choosing a relative large slice thickness. TR and TE allowed for T<sub>2</sub>-weighted contrast while one whole image is acquired in one TR.

The volume obtained during acquisition consisted of 11 coronal slices. One volume covering the entire anatomy is defined as one dynamic. The volume was scanned 60 times covering multiple respiratory cycles, e.g. 60 dynamics were acquired. The acquisition of more dynamics results in more scanned volumes, increasing acquisition time.

The built in navigator was planned on the right hemidiaphragm. Each navigator

acquisition precedes the acquisition of each image and is used for image sorting according to its respiratory state. The total acquisition (both navigator and images) was done under free breathing for 6 minutes with an temporal resolution of 1.7 image frames per second. This resulted in an image acquisition frequency suitable to obtain snap shots of respiratory states.

An acquisition scheme is shown in figure 17, for illustrative purposes a volume of 6 slices is displayed in the enlarged box. In the left part, the navigator acquisition is plotted over time and the respiratory trace can be determined. An arbitrary part of the respiratory signal is shown enlarged (right), illustrating the alternating acquisition method where a navigator precedes each image acquisition. The multiple 2D acquisition acquires sequentially each slice, however as illustrated in the right figure these slices are not acquired contiguous but interleaved. This interleaved acquisition prevents cross talk between adjacent slices and allows for a high temporal resolution.

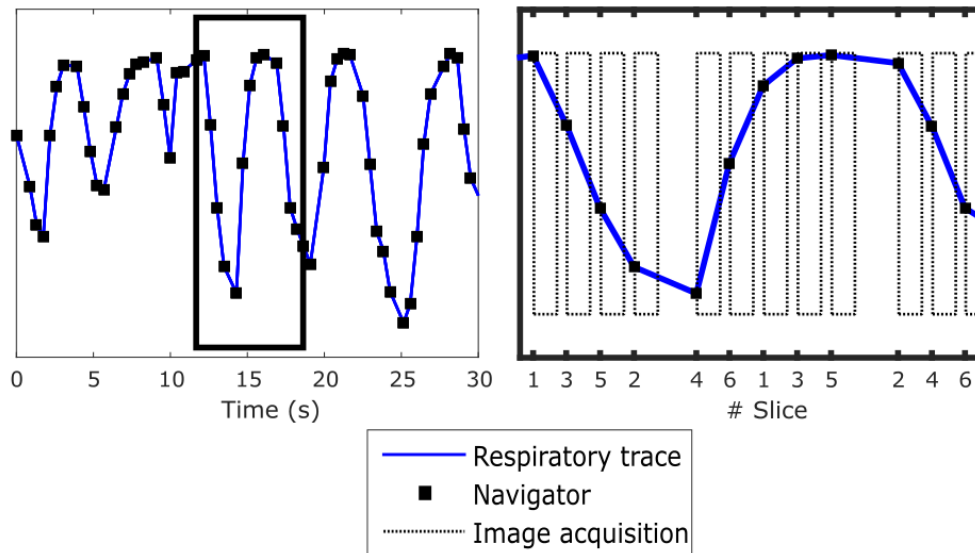


**Figure 17:** Illustration of image acquisition using a navigator (■) and interleaved acquisition mode. The respiratory trace is determined by fitting a line trough all navigator points. The black box in the left figure is shown enlarged at the right. The volume illustrated consists of 6 slices and the volume is not acquired contiguously. Each slice acquisition is coupled to a preceding navigator for respiratory binning.

## 2.2 Retrospective sorting of images

After acquisition, the stack of 2D slices was sorted into 10 3D volumetric images according to their respiratory state (bin). The 1D navigator registers the position of the diaphragm before image acquisition and is used for respiratory motion tracking.

The navigator is used in two steps. First, the position of the diaphragm can be used to reconstruct the respiratory trace and second the image acquired directly after the navigator can be assigned to a respiratory state, called synchronization of the respiratory trace with image acquisition. The synchronization of the respiratory trace with image acquisition is mandatory for image sorting. Therefore, the navigator allows for respiratory binning without the use of internal or external surrogates for breathing motion as is common for CT. The respiratory state was defined using the navigator and determined by two different methods, amplitude and phase binning.

### 2.3 Phase & Amplitude binning

The binning of images was performed using an in-house developed program written in Matlab (The Mathworks Inc., Natick, MA). This program divides the respiratory trace in 10 respiratory bins analogous to the 4D-CT method currently used at the AMC and assigns each image to its corresponding bin. Phase binning is the most frequent used method of retrospectively sorting images according to respiratory motion. This method uses the local maximum (end-exhale position) of the waveform as the start of the first bin, see figure 18a. All end-exhale positions were calculated using a peak detection algorithm with the use of the navigator derived respiratory trace. The whole respiratory trace is thus divided in single respiratory cycles from one end-exhale positions to the other, as shown in figure 18a by the vertically dashed lines.

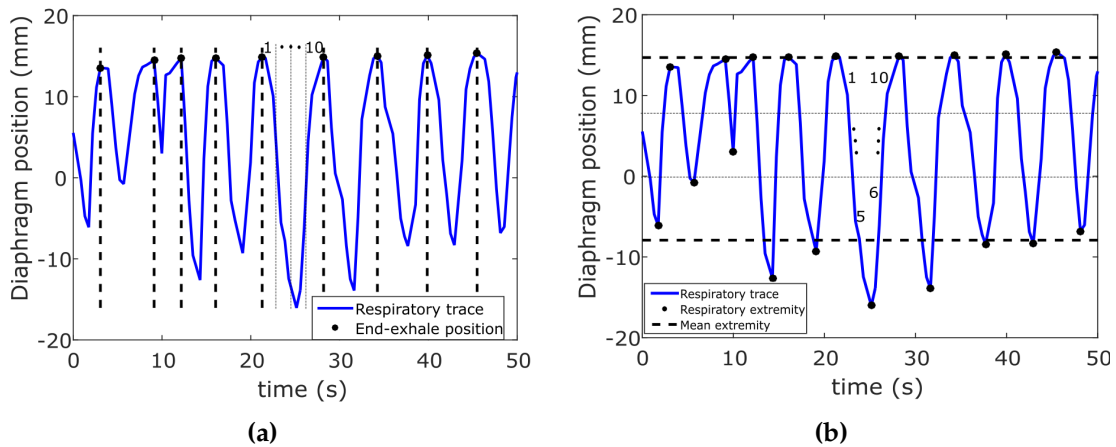


**Figure 18:** A representation of (a) phase and (b) amplitude binning. The numbers inside the figure represent the determined bin for that position. Phase binning determines bins by using the respiratory cycle between end-exhale position while amplitude binning uses a range of actual diaphragm positions.

In phase binning the first bin consists of the first 10% of the respiratory cycle and this continues until bin 10 which covers the last 10% of the respiratory cycle. Each respiratory cycle is divided in 10 equidistant parts representing the phase of the

respiratory cycle, see figure 18a. By assigning a respiratory phase to the navigator, the image acquired after the navigator can be assigned to its respiratory state. This respiratory state is sorted to its corresponding respiratory bin. In this manner, all acquired images were sorted into its respective bins according to the respiratory phase in which each preceding navigator resides.

As explained in part I, phase binning is very sensitive to breathing irregularities like variation in inhalation volumes, respiratory frequency and amplitudes. A different type of method based on the amplitude of the respiratory trace could potentially improve the accuracy of retrospective sorting and counter variability in breathing over larger imaging periods. Amplitude binning uses the amplitude of the respiratory trace (i.e. the diaphragm position) instead of the respiratory phase for sorting of images. Amplitude binning has the potential to reduce artifacts in the acquired 4D data set and the variation within volumes are expected to be lower [15,24,47].

For amplitude binning, both end-exhale and end-inhale positions are determined using peak and trough detection algorithms. A mean value for the amplitude of these extremities was calculated, as shown in figure 18b (the dashed horizontal lines). The range acquired between the calculated mean extremities was used for binning and divided in 5 equally distributed amplitude bins. The amplitude range causes outliers in the breathing signal to be omitted.

It is known that internal motion of organs or tumors follow an elliptical path in the SI direction, with inhale and exhale trajectories being different [48]. The difference of these motion trajectories has been referred to as hysteresis. The amplitude binning method accounts for hysteresis by determining the slope of the respiratory trace. Identical amplitudes with different slopes are treated differently and were assigned to a different bin, see figure 18b. The difference between exhale and inhale is considered by calculating the sign of the slope of the respiratory trace. A positive sign is exhalation and a negative sign is inhalation. Only the sign of the slope is considered and not the magnitude because the difference between inhalation and exhalation has the largest impact on hysteresis and consequently organ movement.

## 2.4 4D data set reconstruction

During binning an image is discarded or assigned to a respiratory bin. Figure 19 shows the result of the binning process. After sorting, from each bin an image at each slice position was selected for the reconstruction of the respiratory correlated 3D volumes.

Figure 19A illustrates that a complete volume of a respiratory state consist of  $N_s=11$  slices. The total of 10 bins should contain a complete volume and this resulted in 110 available image state positions. However, due to the process of binning, multiple images can be assigned to the same slice position and respiratory bin. This redundancy is depicted in figure 19B in for example bin 1, slice position 2. For the reconstruction of the most representative 4D-MRI dataset, an image had to be selected from multiple images at a slice position at a certain bin. This was done by selecting the image with

the median diaphragm position.

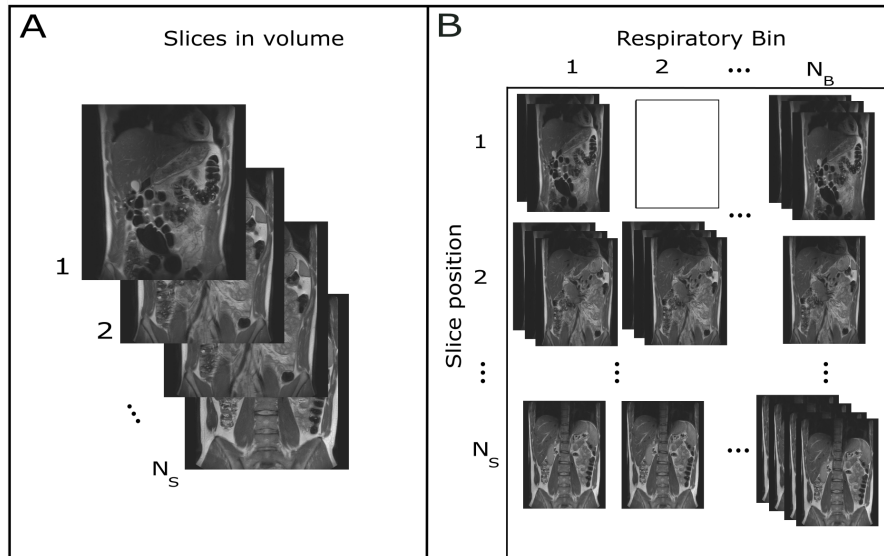


**Figure 19:** The volume containing  $N_s=11$  slices (A) and the result after binning (B). The redundancy of slices is shown where multiple images are assigned to the same slice position and respiratory bin. Slice position 1 at bin 2 is missing, which results in an incomplete 4D-MRI dataset.

To select the image with the median diaphragm position for 4D data set reconstruction, a region of interest (ROI) was defined on the right diaphragm. Figure 20 shows the steps of this procedure. The ROI, see figure 20A, was used to extract the diaphragm. The cropped image was turned binary to enhance the contrast between the diaphragm and the lungs filled with air.

By using image processing methods the binary image quality was improved. The mathematical morphology operation 'opening' was followed by the mathematical morphology operation 'closing' to obtain the image as shown in figure 20B. This filter was implemented with a mask in the shape of a circle with radius (1 cm), resulting in the elimination of noisy components and a smooth diaphragm shape [49].

The position of the diaphragm was determined relative to the first image in the set of redundant images using a rigid registration method that only applies translational transformations. This method determines a translational vector that registers the two images. The vector shows the geometric transformation that aligns each image intensity based on the reference image. The y-component of this vector is a parameter for the position variation in the SI direction, which is the relative diaphragm position. Figure 21 shows the relative diaphragm position obtained from a representative slice. From the set of relative diaphragm positions ('plus'), the image with the median diaphragm positions ('bullet') was selected for the construction of the 4D-MRI data set.

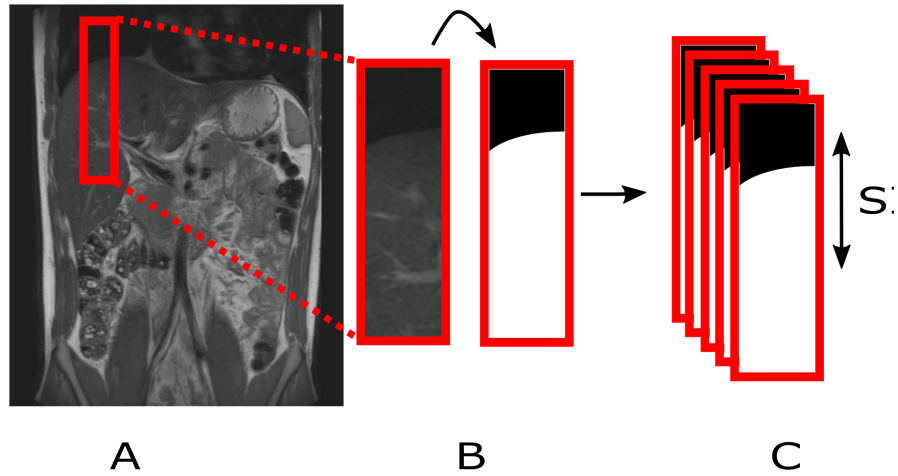


**Figure 20:** Extraction of images for 4D-MRI data set reconstruction by determining the median diaphragm position. The selected ROI (A) is turned binary (B) and the SI movement is extracted using a rigid registration algorithm(C).

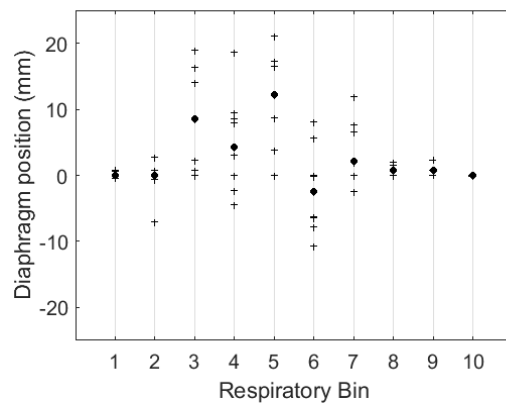


**Figure 21:** Median diaphragm selection of all bins of a representative slice. The selected median (•) as well as the redundant data (+) is shown. The image at position zero is the randomly chosen first image of the redundant images and not correlated to a low variation.

## 2.5 Analysis

The scans acquired for the 4D-MRI data set are optimized for imaging of the pancreas. The diaphragm reflects directly a respiratory state. Variations of the diaphragm in the resulting 4D-MRI are thus a measure for the quality of binning. This is the

reason that for analysis we focused on the position, shape and motion of the diaphragm instead of characteristics of the pancreas. After reconstruction of the 4D-MRI data sets the result was evaluated on several aspects:

- Variability of diaphragm position inside the same bin and slice position
- Respiratory induced diaphragmatic motion
- Smoothness of anatomical structures within a 3D-volume
- 4D-MRI dataset completeness

### **Variability of diaphragm position**

The diaphragm position was not only used to select the appropriate image for 4D dataset reconstruction. As the images were binned according to their respiratory state, all images at a slice position of a certain bin should consist of approximately the same diaphragm position. From the redundant images the variation in diaphragm positions is a measure of the accuracy of the binning method. This variation was determined from three central slices covering the largest diaphragm motion. The mean variation was determined by averaging the standard deviation (SD) for all 10 respiratory states of these three central slices, resulting in the mean SD. The standard deviation was calculated by:

$$SD = \sqrt{\frac{1}{N} \sum_{i=1}^N (x_i - \mu)^2} \quad (7)$$

where N is a number of redundant images,  $x_i$  the diaphragm position and  $\mu$  the average diaphragm position.

This allowed to compare the accuracy of both amplitude and phase binning. Image positions in the 4D-MRI dataset containing only one image were excluded from intra-bin variation calculation as no redundant images were found at these positions. Also, the worst case scenario (called the maximum SD) is reported by determining for all volunteers the maximum variation in the three central slices.

### **Respiratory induced diaphragmatic motion**

From the resulting 4D-MRI, the difference in diaphragm position between bin 1 and bin 5 represent the median respiratory motion from begin-inhale to end-inhale. The median diaphragmatic motion was determined for each volunteer by calculating the largest displacement of the diaphragm for three central slices. The median diaphragmatic motion is defined as the peak-to-peak (PKP) magnitude. The inter-bin variability is determined by analysing the diaphragm motion during respiration for hiccups.

The percentage of outliers is calculated for the amplitude binning method. An outlier is defined as the part of the respiratory cycle (and the corresponding images)

that is not in the defined amplitude range, see figure 18b. These images are discarded and the percentage outliers ( $O_{ampli}$ ) is calculated as:

$$O_{ampli} = \frac{N_O}{N_{mri}} \quad (8)$$

where  $N_{mri}$  is the total number of images obtained from scanning and  $N_O$  the number of excluded images. Phase binning does not define a binning range and therefore does not exclude images,  $O_{phase}$  is 0.

### **Diaphragm shape**

A visual representation of the diaphragm shape was obtained by reconstructing a 3D-volume in the sagittal plane. The sagittal reconstruction is changing the view of the 3D volume images in each bin. From the acquired coronal images an image of the sagittal plane was obtained.

From each 3D volume inside a bin the diaphragm shape was determined using a similar image processing method as used for median selection. The diaphragm of each image was registered to each first slice in a volume. A 1D representation of the diaphragm shape orthogonal to the image plane can be obtained using this method. The shape of the diaphragm was used to evaluate the influence of variability on the final 4D-MRI set.

### **Data set completeness**

Another important factor of retrospective binning is shown in figure 19B, slice position 2 from bin 2 is left unassigned. The unassigned position is the consequence of the process of binning and has a direct impact on the completeness of the final 4D-MRI dataset.

The process of binning is dependant on multiple factors like breathing period, breathing amplitude and image acquisition frequency. Beforehand, it is not evident at what state in the respiratory cycle an image is acquired. It is possible that the respiration cycle (3-7 s) has a similar period as the acquisition of images (6.2 s), leading to the acquisition of a slice position at the same respiratory state for most of the dynamics. This uncertainty leads to incomplete datasets as not all slice positions can be assigned to all respiratory states. These missing images could deteriorate the quality of the 4D-MRI data set.

The probability of missing slices decreases with increasing scan time. In other words, to increase the data completeness more dynamics have to be acquired during image acquisition. This however increases acquisition time which is an important aspect in the clinic and should be as low as possible. To assess the influence of acquisition time we evaluated the relation between number of dynamics (D) and data completeness (C). Data completeness is quantified as the percentage of filled image positions ( $N_I$ ) of the total available image positions ( $N_T$ ):

$$C = \frac{N_I}{N_T} = \frac{N_I}{N_S * N_B} \quad (9)$$

where  $N_S$  is the number of slices in a volume, see figure 19 and  $N_B$  the number of respiratory bins.

Data completeness was simulated using data acquired from a single volunteer, 200 dynamics were acquired during image acquisition. Subsets of dynamics were obtained containing different number of dynamics in the range of 1-100 dynamics. A subset was selected by choosing the required amount of dynamics randomly from the original 200 dynamics. This allowed us to simulate 4D-MRI datasets for each subset of dynamics. Each simulation yielded a value for data completeness related to the number of dynamics. C and D were calculated and the relation between the two was studied. To determine the variation on C each simulation was repeated 10 times, varying the distribution over 200 dynamics.

### 3 Results

4D-MRI volumetric datasets were successfully acquired with T2-weighted contrast. The obtained T2-weighted images facilitates abdominal structure contrast and potentially tumor-tissue contrast. The resulting 4D-MRI consisted of 10 respiratory bins with in each bin a 3D volume of 11 coronal slices.

#### 3.1 Variability of diaphragm position

**Table 1:** Amplitude and phase binning results. The mean standard deviation and maximum (max.) standard deviation for 12 volunteers.

Volunteer	Amplitude Binning		Phase Binning	
	Mean SD (mm)	Max. SD (mm)	Mean SD (mm)	Max. SD (mm)
1	0.7	2.0	0.9	1.8
2	1.1	1.7	4.3	10.9
3	0.4	0.7	1.2	2.3
4	0.8	1.7	1.9	4.9
5	0.9	2.0	2.5	5.6
6	0.6	1.7	1.4	3.1
7	0.8	1.5	2.6	5.6
8	0.7	1.3	2.6	4.5
9	0.9	1.7	3.7	10.2
10	0.6	1.8	2.5	5.1
11	0.8	2.0	1.9	4.1
12	0.6	1.3	1.5	3.8
<b>Mean</b>	0.7	1.6	2.3	5.2

Table 1 shows the mean standard deviation (mean SD) and the maximum standard deviation (max. SD) for both binning methods. Also, the mean values of these parameters from all volunteers are given. We found that the variability for amplitude binning is lower than for phase binning for both the mean SD and the max SD. The mean standard deviation for 12 volunteers was found to be 0.7 mm and 2.3 mm for amplitude and phase binning, respectively. The maximum standard deviation was found to be 1.6 mm and 5.2 mm for amplitude and phase binning, respectively. Over all volunteers, the intra-bin variability is approximately a factor 3 smaller for amplitude binning than for phase binning.

### 3.2 Respiration induced diaphragmatic motion

Figure 22 shows the variability for all bins of a representative slice (slice 7). Also, the image selected for 4D-MRI reconstruction are shown as black dots (●). The variation for phase binning is clearly higher than amplitude binning in 8 out of 10 bins. The figure shows that for phase binning the higher variation leads to a deviating respiration induced diaphragmatic motion. The median image selected for the 4D-MRI data set as proposed herein results for phase binning in a discontinuous respiratory motion. This in contrast to amplitude binning which shows no hiccups in the diaphragm position (linear inhale and linear exhale).

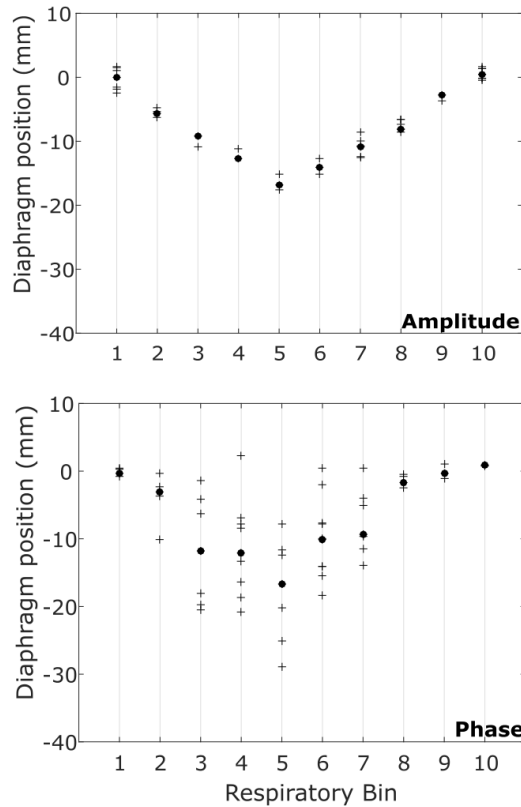


**Figure 22:** Diaphragm position of all images binned to a representative slice of a volunteer. The redundant images (+) as well as the selected median image for the 4D-MRI data set (●) is depicted. The position is determined by registering all diaphragms to an arbitrary slice at begin of inhalation (bin 1).

Table 2 presents the peak to peak magnitude from begin inhalation to end-inhalation of each volunteer. For amplitude binning the percentage of outliers excluded by the defined amplitude range is also shown. The PKP distance (SD) is 11.9 (4.1) mm and 13.5 (6.0) mm for amplitude and phase binning, respectively. Again, a larger variation was found for phase binning with a higher deviation of the PKP magnitude. The PKP magnitude for phase binning is dependant on the image selected for reconstruction. If

**Table 2:** Peak to peak (PKP) magnitude of the diaphragm for both binning methods. The outliers ( $O_{ampli}$ ) excluded by the amplitude binning method is also shown.

Volunteer	Amplitude Binning		Phase binning
	PKP (mm)	$O_{ampli}$ (%)	PKP (mm)
1	5.1	19.4	4.5
2	20.8	22.3	27.4
3	7.1	20.6	7.8
4	12.7	20.8	11.8
5	14.9	22.1	16.2
6	10.5	17.2	11.8
7	12.6	21.2	17.7
8	11.6	23.4	13.3
9	15.2	23.1	19.7
10	12.5	20.6	11.7
11	10.9	18.3	10.8
12	9.1	16.8	10.1
Mean	11.9	20.5	13.5
SD	4.1	1.9	6.0

PKP= peak to peak magnitude

another image is selected for 4D reconstruction the PKP magnitude will deviate, see figure 22. For phase binning the large variation influences the PKP magnitude.

On the other hand, for amplitude binning the PKP magnitude is dependant on the defined amplitude range for binning. Outliers are excluded by the range and the result is a lower PKP magnitude. The average (SD) of  $O_{ampli}$  is 20.5 (1.9)% for amplitude binning, which indicates that amplitude binning is a representation of 80.5% of the respiratory motion.

### 3.3 Diaphragm shape

The artifact present in the final 4D-MRI dataset were investigated for both binning methods. The resulting 3D volumes in each bin were therefore studied and the influence of the variation on the data set illustrated. As shown in figure 23A each respiratory bin consists of 11 slices. During acquisition, the images are acquired in a coronal orientation. Multi-planar reconstructions, or the reconstruction in another plane is performed to analyse the out of plane result. Figure 23B, shows the sagittal reconstruction of a representative bin.

The discontinuous shape is an artifact of the 4D-MRI reconstruction method as the anatomy of the diaphragm is smooth. In figure 23B, the reconstruction of the diaphragm results in a smooth diaphragm shape for amplitude binning while for phase

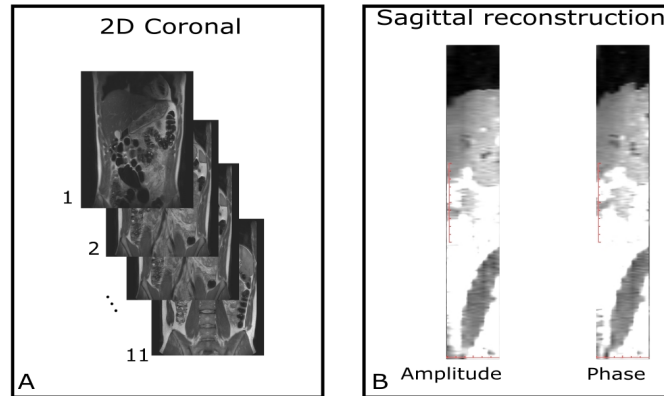


**Figure 23:** 4D-MRI dataset result (A) showing a volume consisting of  $N_s=11$  coronal slices and a sagittal reconstruction (B) from this bin at the position of the diaphragm.

binning the diaphragm is discontinuous.

The determination of the 1D-diaphragm shape of bin 1 and bin 5 are shown in figure 24. Each diaphragm position is determined by rigid registering it to the first image in a bin. Figure 24a shows that for bin 1 (begin-inhale) the diaphragm has smooth shape and amplitude and phase binning are similar. However, for bin 5 (end-inhale) the diaphragm shape is not similar and amplitude binning has a smooth shape while phase binning shows a discontinues diaphragm shape.

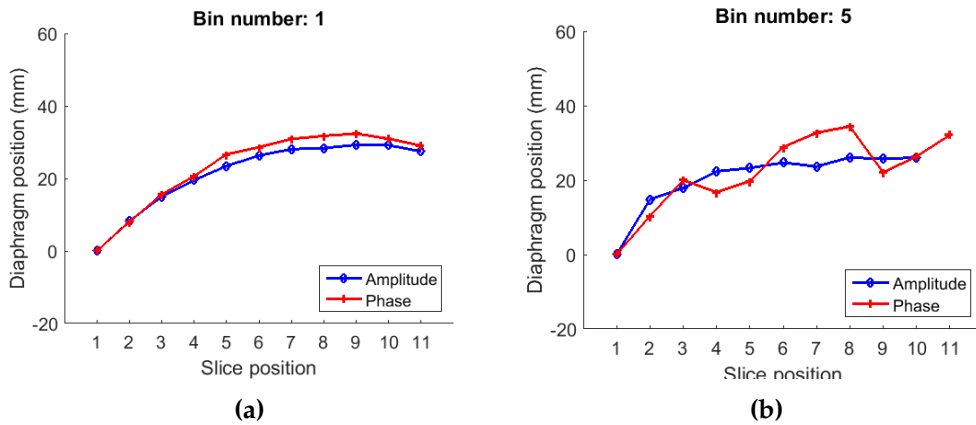


**Figure 24:** The diaphragm shape using rigid registration methods for bin 1 (a) and bin 5 (b) of a representative volunteer. For bin 1 the diaphragm shape is very similar for both methods while for bin 5 the diaphragm is different. The shape of the diaphragm for phase binning is more discontinuous than for amplitude binning.

**Table 3:** Data completeness (C) for both binning methods

Volunteer	Amplitude binning	Phase binning
	C (%)	C (%)
1	96.4	100
2	92.7	100
3	93.6	99.1
4	90.0	99.1
5	95.5	100
6	96.4	100
7	96.4	100
8	96.4	98.2
9	93.6	100
10	96.4	100
11	97.3	100
12	96.4	100
Mean	95.1	99.7

### 3.4 Data completeness

Table 3 shows the data completeness (C) for all volunteers. Phase binning showed a mean C of 99.7% while amplitude binning obtained an average C of 95.1%. For phase binning a complete dataset for 10 out of 12 volunteers was obtained while amplitude binning did not achieve 100% completeness. We found that for amplitude binning the range of C was 90-97.3% while for phase binning the range was 98.2-100%.

Figure 25a shows for amplitude binning for each bin the accumulated missing images for all volunteers. Figure 25a shows that bins 4 and 5 have more missing images than other bin positions. 11 out of 12 volunteers show at least one missing image in bin 5. For all volunteers, the sum of total missing images for bin 4 is 14 and for bin 5 is 26. The range of missing images for the other bins is 0-6 and the standard deviation of all bins is 7.9. This in contrast to the missing slices shown in figure 25b. No slice dependency was found and the range of missing images per slice was 2-8, with a standard deviation of 2.3 images. This indicates that a strong dependency on bin number to the missing images is observed in contrast to the slice number where no such dependency is found.

Figure 26 shows the result of the data completeness (C) simulation. Each subset of dynamics ranging from 1-100 is displayed with steps of 5 dynamics. The mean value of the 10 simulations (bullet) is shown and the error bars are the standard deviation. The value for C increases more rapidly per dynamic for phase binning compared to amplitude binning.

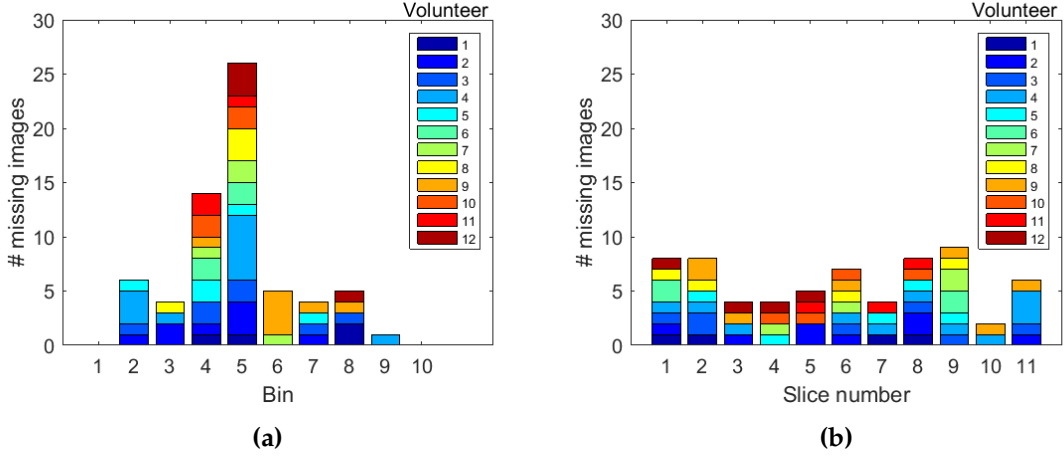


**Figure 25:** Diagram containing the accumulated number of the missing images per (a) bin and per (b) slice for all volunteers.

Both binning methods show a relation similar to the formula:

$$C = 100(1 - e^{-KD}) \quad (10)$$

where  $K$  is a binning method dependent constant and  $D$  is the number of dynamics. The exact value for  $K$  is not directly evident and dependent on multiple factors like  $N_s$ ,  $N_b$ , breathing phase and breathing amplitude of the volunteers. However from figure 26 it is clear that  $K_{amplitude} < K_{phase}$  and  $2K_{amplitude} \approx K_{phase}$ . To achieve same values for  $C$ , amplitude binning should acquire more dynamics than phase binning.

The value for  $K$  is patient dependent and patient specific approximation of  $K$  can be obtained by fitting equation 10 to the model.  $K_{amplitude}$  was found to be 0.065 and  $K_{phase}$  was found to be 0.12, see figure 26 for the fit.

In the presented volunteers, the sequence settings (e.g. 11 slices, no cardiac triggering) resulted in a scan duration of 6 minutes to acquire 60 dynamics. The acquisition of 60 dynamics results for both methods in sufficient  $C$ , since the plateau is reached and the largest change in slope has occurred. After 60 dynamics, the increase in the number of dynamics has a relatively small gain in  $C$  for both methods. It should be noted that since we used 60 dynamics, the acquisition time for phase binning can almost be reduced by a factor 2. For phase binning to obtain sufficient  $C$  the total amount of dynamics can be decreased to 30 dynamics due to the larger value for  $K_{phase}$ .

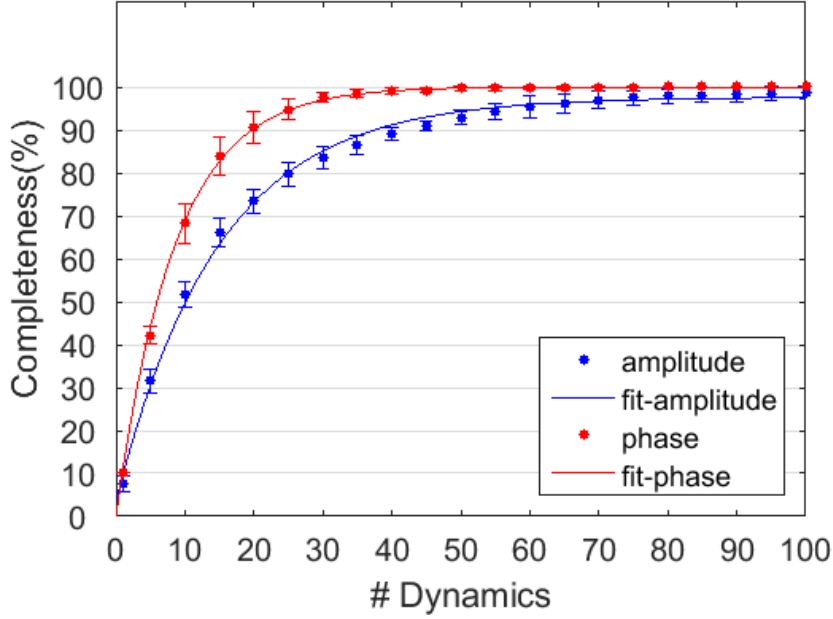


**Figure 26:** 10 simulations of data completeness for every 5 dynamics. The standard deviation of each simulation is plotted as the errorbar. The fit according to the equation 10 is also shown for  $K_{amplitude} = 0.065$  and  $K_{phase} = 0.12$ .

## 4 Discussion

In this work, I presented a 4D-MRI method analogous to 4D-CT, and explored both phase binning as well as amplitude binning to sort images according to their respiratory state.

### Phase binning

The variability found in phase binning is compared to the established 4D-CT and other 4D-MRI methods. The variation of my method had a range of 0.9-4.3 mm standard deviation with a 2.3 mm mean. These values are similar to position variations of phantom simulations performed in a 4D-CT with a range of 0.8-4.6 mm depending on respiratory wave form [50]. Also, the comparison with another 4D-MRI method based on phase binning shows similar values of variation where the mean variation was 2.5 mm [40]. This gives the confidence that the phase binning method implemented is correct and with a similar variability as compared to earlier findings.

The strength of phase binning is its simplicity and efficient use of available data. The simplicity of phase binning is reflected in the choice of respiratory surrogates.

The common methods of respiratory motion tracking are external monitoring devices like pressure belts or reflective markers. These markers only measure a surrogate of the respiratory motion based on the expansion and contraction of the abdomen. These surrogates are placed on the thorax or the abdomen and are based on the assumption that there exists a good correlation between the motion of the surrogate

and internal structures. In literature, a good correlation is often found. Still, the correlation is susceptible to marker placement and tumor or organ motion should not rely only on external marker information [51, 52]. Moreover, most external surrogates often automatically adjust the gain (calibration) to generate a reproducible respiratory trace. This causes these external monitoring devices to be very suitable for phase binning. However, it excludes amplitude binning because the calibration omits the possibility of respiratory amplitude determination.

Phase binning uses each respiratory cycle for the binning of images. This efficient use of data results in fast acquisition times or high data completeness. However, it does not account for irregular breathing. Phase binning will assign an image of shallow inhalation in the same bin as deep inhalation. Logically, a very deep inhalation will have an impact on the anatomical positions of internal organs resulting in an artifact in the final 4D-dataset. In short, phase binning does not account for irregular breathing.

### **Amplitude binning**

The amplitude binning method proposed herein has the potential to account for irregular breathing by binning the image according to the actual diaphragm position instead of the respiratory phase. The actual diaphragm position is needed instead of a calibrated respiratory trace obtained by a respiratory surrogate. The use of the navigator does not depend on a surrogate and determines the exact position of the diaphragm prior to each image acquisition. This is a more accurate representation of the respiratory motion than the respiratory surrogates as the actual diaphragm motion is acquired. Also, navigator derived diaphragmatic motion is found to correlate better with pancreatic motion than respiratory bellows [37]. Finally, besides that the navigator allows for amplitude binning, it facilitates the synchronization of images with the respiratory trace.

The low variation found in amplitude binning confirms that amplitude binning has eliminated outliers delivering a smooth diaphragm shape and a linear breathing signal. A qualitative analysis of the diaphragm shape was performed. Amplitude binning resulted in a smoother diaphragm shape than phase binning especially for the bins around end-inhalation (3-7) as illustrated for bin 5 shown in figure 24. This means that the variation is dependent on the respiratory state, which is confirmed by figure 22 where the variation in bin 3-7 is substantially higher than in the other bins.

The dependency of variation per respiratory state is due to respiration physiology, where the variation of end-inhale positions is larger than the variation of end-exhale positions, see figure 18. This results in a more stable diaphragm shape at bin 1, see figure 24a. Both methods result in a continuous diaphragm shape at begin-inhalation.

This in contrast to bin 5 where a larger variation is present. Because amplitude binning does not sort images according to the phase of the respiratory cycle the potentially large differences in respiration physiology are not affected by differences in variation. This is illustrated in figure 24b, where the diaphragm shows discontinuities caused by variation in the phase binning method, which are not found in the amplitude

binning method.

The reduced variability of amplitude binning comes with a price. The data completeness for 60 dynamics is lower for amplitude binning than for phase binning. The range used during amplitude binning, see figure 18b results in less available images for binning and consequently in lowered data completeness. The 60 dynamics implemented in the current sequence optimization step resulted for amplitude binning in a mean data completeness of 95.1%. The missing data is dependent on the bin number while it is not dependent on the slice position in the volume, see figure 25. The bin dependency of missing slices is attributed to the patient's physiology. Inhalation motion is faster than exhalation motion [53]. This physiology combined with the larger variation in end-inhale positions contributes to a larger fraction of missing images in bin 4 and 5. More images are acquired during exhalation than during inhalation which is the reason for the increased number of missing images in bin 4 and 5.

The dependency of the binning method and the missing images in a bin could raise problems when the data completeness does not suffice. This problem is shown for volunteer 4, with a data completeness of 90% where 6 images are missing in bin 5, see figure 25a. The influence on delineation on the ITV is not directly evident, however there is a high probability that important structures at end-inhalation (bin 5) are missing in the 4D-MRI. A solution for this problem could be to track the data completeness, where the range is defined during acquisition and binning is performed continuously. The acquisition could then be terminated when a sufficient data completeness is achieved.

### **Amplitude vs Phase binning**

The 4D-MRI method presented in this thesis can both deliver phase and amplitude binned 4D-MRI from the acquired scanned images. Phase binning has superior acquisition time compared to amplitude binning because the efficient use of each respiratory cycle. This directly means that during binning all respiratory states, for example very deep inhalation and very shallow inhalation all are included in the 4D-MRI dataset (after selection of the median image).

This in contrast to amplitude binning where outliers are removed by the definition of the amplitude range. The influence of the range on the 4D-MRI data set is that amplitude binning represents the respiratory cycles that are inside this range. The definition of the range is therefore studied. By calculating the mean of the extremities (as explained in figure 18b) a mean of 79.5% of the respiratory cycle is included by the amplitude range. An average 20.5% with SD 1.9% of the respiratory cycle is defined as outliers and not used for the 4D-MRI dataset.

The consequence of this relatively high amount of excluded images is that amplitude binning is a representation of the respiration at the most common states of the respiratory cycle. This is also reflected in the found mean peak to peak motion of the diaphragm, as shown in table 2. The mean peak to peak motion is 11.9 mm for amplitude binning compared to 13.5 mm for phase binning. This number could indicate that the amplitude binning method is an underestimation of the actual respiratory motion of a

patient, which could result in an underestimation of the ITV. This aspect of amplitude binning should be investigated to assess the influence on the resulting ITV.

Still, it does not directly exclude amplitude binning as a suitable method. One should keep in mind that the variability of phase binning really inhibits exact definition of the respiratory motion, as it is dependant on the selection of an image from a highly variable data set. Therefore, the 4D-MRI dataset obtained by phase binning has more artifact creation due to irregular breathing patterns. This variation in the phase binning method is not predictable and can not be excluded. This in contrast to the amplitude binning method where definitions of the amplitude range and bin size are user controlled parameters.

A 4D-MRI data sets of both methods can automatically be acquired after image acquisition and both methods can be implemented in the clinical workflow. For amplitude binning, the representation of the respiratory cycle is very suitable to track the average organ movement during respiration. The percentage of unused data can be reduced by increasing the amplitude range acquired for binning. However, the increase of the amplitude range has negative consequences on data completeness as the outliers are less present during acquisition. To avoid a lowered data completeness, the number of bins could be decreased to 6 or 8 respiratory states. A thorough analysis should be performed on the influences of increased bin size on the resulting 4D-MRI data set combined with a different number of respiratory bins.

#### **4D-MRI vs 4D-CT**

The  $T_2$ -weighted contrast achieved by the 4D-MRI method could be used for accurate delineation of abdominal structures. However, the 4D-MRI method has some differences to the 4D-CT currently used in clinical practice.

First of all, the acquisition of 4D-CT images is acquired in cine mode. This means that each slice or table position is measured for the whole respiratory cycle before continuing to the next table position. This cine-acquisition of the CT, results in the fast acquisition of high-resolution images and a complete 4D-data set. For the 4D-MRI method, the dependency of binning on the respiratory signal to is a less controllable parameter where the data completeness is not directly evident. The MRI images are acquired continuously without feedback from the respiratory signal which lead to the uncertainty of missing images. However, with sufficient acquisition time sufficient data completeness can be achieved by reducing the probability of missing images. This was confirmed by the data completeness simulation shown in figure 26. In contrast to CT, MRI does not use ionizing radiation so tailoring the acquisition time to achieve sufficient data completeness has no direct consequence for the patient other than prolonged acquisition time.

Second, the CT images are always obtained in a transverse orientation with high out of plane resolution (1.25 mm). In contrast, the MRI images used with 2D-acquisition have compromised out of plane resolution (5mm) to ensure adequate SNR. The clinical consequence is two-fold. First, multi-planar reconstructions are from low quality.



**Figure 27:** Delineation of the pancreas on coronal acquired 4D-MRI dataset. The delineated pancreas of bin 1 (yellow), bin 5 (purple) and bin 10 (pink) are shown superimposed on the image of bin 1.

Second, delineation of organs or tumor on the 4D-MRI are restricted to coronal images.

Figure 23 shows the influence of low out of plane resolution. The reconstruction with low resolution results in so-called stitching artifacts, where each transition from one slice to the other is not continuous. Multi-planar reconstructions of the 4D-MRI data set are not suitable for delineations of organs and tumors as they require a high resolution.

On the other hand, the delineation of organs and tumors is commonly done on images of the transverse plane because the golden standard CT only acquires axial images. Radiation Oncologist are thus accustomed to axial delineations. To delineate on the acquired 4D-MRI data set the coronal acquired images should be used. A coronal delineation of the pancreas was performed at our institution on one volunteer. A physician delineated the pancreas on all bins of the 4D-MRI data set. The contours of the delineated pancreas of bin 1, bin 5 and bin 10 are shown in figure 27 superimposed on MR image of bin 1. The respiratory induced motion is clearly visible.

It was feasible to delineate the pancreas on all volumetric images and the respiratory motion of the pancreas can be tracked. From these images, an ITV can potentially be obtained. The 4D-MRI could aid in the accurate determination of respiratory induced motion of the tumor when it is combined with high quality MRI image of a pancreatic tumor. The co-registration of a good visibility of the tumor, together with the accurately determined pancreatic motion of the 4D-MRI could lead to an accurate ITV.

Still, the accurate delineation and motion of the pancreas and pancreatic tumors on MRI should be assessed on multiple patients. The MRI aided ITV determinations should be compared to the golden standard of CT and 4D-CT. Moreover, the comparison of delineations on coronal images should be compared to the golden standard of axially

acquired 4D-CT images. Future studies should focus on the influence of 4D-MRI on ITV determination and delineation accuracy. This comparison to the 4D-CT will quantify the possible advantages of the developed 4D-MRI for clinical implementation.

## 5 Future outlook

4D volumetric images were obtained that could allow for accurate abdominal structure delineation and motion management. The accurate delineation of organs and tumors could result in the reduction of margins and aid in the treatment of tumors. The advantage of the 4D-MRI method per tumor site needs to be quantified to allow for reduced margins. The influence of the T<sub>2</sub>-weighted images on systematic delineation errors is a subject undergoing intense study at our institution and should be determined to define a more accurate margin around the CTV.

The more accurate amplitude method could aid in defining more accurately the internal margins with less uncertainty. Still, one should realize that the amplitude derived 4D-MRI dataset does not show the outliers. The patient does take an occasional deep breath and this information is excluded for amplitude binning. The influence of the exclusion of these respiratory states should be assessed. For example, the influence on the dose distribution to the tumor and organs at risk should be calculated and compared to the current 4D-CT calculations. An accurate determination of the influence of differences in bin size and bin number could aid in the improvement of the developed 4D-MRI sorting algorithm.

We also propose to calculate for each patient the time spent at each breathing amplitude. The probability of each amplitude bin can be calculated accordingly. Using this definition a more accurate value for the amplitude range could be determined. The altered range could lead to more meaningful definitions of inhalation and exhalation instead of the mean end-exhale positions and mean end-inhale positions used in this research.

Moreover, the accurate determination of the time spent at each diaphragm position could aid treatment planners in understanding the probability of a certain respiratory state leading to a more robust treatment plan.

Finally, the focus of sequence optimization was focused on the pancreas. Only clinically available scanning protocols were used which allows expansion to other structures due to the versatility of the MRI modality. Organs like the liver, esophagus and stomach are areas of interest and respiratory motion management of these organs can possibly be improved by 4D-MRI. A successful optimization step on the esophagus has been performed where also the cardiac movement is considered by using cardiac triggering. Further optimization and validation of this sequence could be beneficial for tumor treatment in the upper abdominal area.

## 6 Conclusion

We demonstrated the reconstruction of accurate respiratory correlated 4D-MRI as an alternative for 4D-CT. In less than 6 minutes,  $T_2$ -weighted images were acquired with clinically available scan protocols. The 1D navigator interleaved with image acquisition allowed for robust respiratory motion tracking and retrospective sorting of MR images. 4D-volumetric images with both amplitude and phase binning were obtained.

The efficient use of the respiratory cycle leads to a lower acquisition time for phase binning compared to amplitude binning. However, amplitude binning showed less variation than phase binning, leading to a more accurate binning method where fewer artifacts are present in the 4D volumetric data set. Moreover, in amplitude binning the image selected for 4D-MRI reconstruction is not hindered by large variations inside each bin delivering user controlled 4D-MRI datasets.

An amplitude binned 4D-MRI with sufficient data completeness leads to the next step in the respiratory management of abdominal tumors. The accurate 4D-MRI could be integrated in the clinical workflow, potentially reducing safety margins and leading to better tumor treatment outcome and less toxicity to the patient.

## References

- [1] Nos.nl, "Kanker nog altijd doodsoorzaak nummer 1," 2015.
- [2] IKNL.nl, "Overleving kanker Nederland," 2016.
- [3] American Cancer Society, "Cancer Treatment Types," 2015.
- [4] Cancer Council Australia, "Radiation therapy," 2015.
- [5] C. F. Njeh, "Tumor delineation: The weakest link in the search for accuracy in radiotherapy," *Journal of medical physics / Association of Medical Physicists of India*, vol. 33, pp. 136–40, oct 2008.
- [6] P. Cherry and A. Duxbury, *Practical radiotherapy: Physics and equipment*. John Wiley & Sons, 2009.
- [7] M. R. Sontag, J. J. Battista, M. J. Bronskill, and J. R. Cunningham, "Implications of Computed Tomography for Inhomogeneity Corrections in Photon Beam Dose Calculations 1," *Radiology*, vol. 124, pp. 143–149, jul 1977.
- [8] E. B. Podgorsak, "Review of radiation oncology physics: a handbook for teachers and students," *Vienna, International Atomic Energy Agency. Educational reports series*, 2003.
- [9] F. M. Khan, *The Physics of Radiation Therapy*. Lippincott Williams & Wilkins, 2010.
- [10] T. J. Jordan and P. C. Williams, "The design and performance characteristics of a multileaf collimator," *Physics in Medicine and Biology*, vol. 39, pp. 231–251, feb 1994.
- [11] J. H. Kim, "LINAC-based High-precision Radiotherapy: Radiosurgery, Image-guided Radiotherapy, and Respiratory-gated Radiotherapy," *Journal of the Korean Medical Association*, vol. 51, p. 612, jul 2008.
- [12] M. van Herk, "Errors and margins in radiotherapy," *Seminars in radiation oncology*, vol. 14, pp. 52–64, jan 2004.
- [13] J. C. Stroom and B. J. Heijmen, "Geometrical uncertainties, radiotherapy planning margins, and the ICRU-62 report," *Radiotherapy and Oncology*, vol. 64, pp. 75–83, jul 2002.
- [14] L. Caravatta, G. Macchia, G. C. Mattiucci, A. Sainato, N. L. V. Cernusco, G. Mantello, M. Di Tommaso, M. Trignani, A. De Paoli, G. Boz, M. L. Friso, V. Fusco, M. Di Nicola, A. G. Morganti, and D. Genovesi, "Inter-observer variability of clinical target volume delineation in radiotherapy treatment of pancreatic cancer: a multi-institutional contouring experience," *Radiation oncology (London, England)*, vol. 9, p. 198, jan 2014.
- [15] J. Ehrhardt and C. Lorenz, *4D modeling and estimation of respiratory motion for radiation therapy*. Springer, 2013.
- [16] C. K. Glide-Hurst and I. J. Chetty, "Improving radiotherapy planning, delivery accuracy, and normal tissue sparing using cutting edge technologies," *Journal of thoracic disease*, vol. 6, pp. 303–18, apr 2014.
- [17] R. Li, J. H. Lewis, L. I. Cerviño, and S. B. Jiang, "4D CT sorting based on patient internal anatomy," *Physics in medicine and biology*, vol. 54, pp. 4821–33, aug 2009.
- [18] T. Pan, T.-Y. Lee, E. Rietzel, and G. T. Y. Chen, "4D-CT imaging of a volume influenced by respiratory motion on multi-slice CT," *Medical Physics*, vol. 31, no. 2, p. 333, 2004.
- [19] M. J. Murphy, J. Balter, S. Balter, J. A. Ben-Como, I. J. Das, S. B. Jiang, C.-M. Ma, G. H. Olivera, R. F. Rodebaugh, K. J. Ruchala, H. Shirato, and F.-F. Yin, "The management of imaging dose during image-guided radiotherapy: Report of the AAPM Task Group 75," *Medical Physics*, vol. 34, pp. 4041–4063, oct 2007.
- [20] T. Yamamoto, U. Langner, B. W. Loo, J. Shen, and P. J. Keall, "Retrospective analysis of artifacts in four-dimensional CT images of 50 abdominal and thoracic radiotherapy patients," *International journal of radiation oncology, biology, physics*, vol. 72, pp. 1250–8, nov 2008.
- [21] U. W. Langner and P. J. Keall, "Quantification of artifact reduction with real-time cine four-dimensional computed tomography acquisition methods," *International journal of radiation oncology, biology, physics*, vol. 76, pp. 1242–50, mar 2010.
- [22] R. George, T. D. Chung, S. S. Vedam, V. Ramakrishnan, R. Mohan, E. Weiss, and P. J. Keall, "Audio-visual biofeedback for respiratory-gated radiotherapy: impact of

- audio instruction and audio-visual biofeedback on respiratory-gated radiotherapy.," *International journal of radiation oncology, biology, physics*, vol. 65, pp. 924–33, jul 2006.
- [23] J. Ehrhardt, R. Werner, D. Säring, T. Frenzel, W. Lu, D. Low, and H. Handels, "An optical flow based method for improved reconstruction of 4D CT data sets acquired during free breathing.," *Medical physics*, vol. 34, pp. 711–21, mar 2007.
- [24] A. F. Abdelnour, S. A. Nehmeh, T. Pan, J. L. Humm, P. Vernon, H. Schöder, K. E. Rosenzweig, G. S. Mageras, E. Yorke, S. M. Larson, and Y. E. Erdi, "Phase and amplitude binning for 4D-CT imaging.," *Physics in medicine and biology*, vol. 52, no. 12, pp. 3515–3529, 2007.
- [25] W. Lu, P. J. Parikh, J. P. Hubenschmidt, J. D. Bradley, and D. A. Low, "A comparison between amplitude sorting and phase-angle sorting using external respiratory measurement for 4D CT," *Medical Physics*, vol. 33, p. 2964, jul 2006.
- [26] E. Rietzel and G. T. Y. Chen, "Improving retrospective sorting of 4D computed tomography data," *Medical Physics*, vol. 33, p. 377, jan 2006.
- [27] D. W. McRobbie, E. A. Moore, M. J. Graves, and M. R. Prince, *MRI from Picture to Proton*. Cambridge University Press, 2007.
- [28] F. A. F. Francisco, A. L. E. de Araújo, J. A. Oliveira Neto, and D. B. Parente, "Hepatobiliary contrast agents: differential diagnosis of focal hepatic lesions, pitfalls and other indications.," *Radiologia brasileira*, vol. 47, pp. 301–9, jan.
- [29] Y. Tang, Y. Yamashita, and M. Takahashi, "Invited. Ultrafast T2-weighted imaging of the abdomen and pelvis: Use of single shot fast spin-echo imaging," *Journal of Magnetic Resonance Imaging*, vol. 8, pp. 384–390, mar 1998.
- [30] D. V. Sahani, "Imaging the Liver," *The Oncologist*, vol. 9, pp. 385–397, jul 2004.
- [31] C. Roth, "Review questions for MRI," 2013.
- [32] T. Henzler, O. Dietrich, R. Krissak, T. Wichmann, T. Lanz, M. F. Reiser, S. O. Schoenberg, and C. Fink, "Half-Fourier-acquisition single-shot turbo spin-echo (HASTE) MRI of the lung at 3 Tesla using parallel imaging with 32-receiver channel technology.," *Journal of magnetic resonance imaging : JMRI*, vol. 30, pp. 541–6, oct 2009.
- [33] R. M. Heidemann, M. A. Griswold, B. Kiefer, M. Nittka, J. Wang, V. Jellus, and P. M. Jakob, "Resolution enhancement in lung 1H imaging using parallel imaging methods.," *Magnetic resonance in medicine*, vol. 49, pp. 391–4, feb 2003.
- [34] K. A. Goodman and C. Hajj, "Role of radiation therapy in the management of pancreatic cancer.," *Journal of surgical oncology*, vol. 107, pp. 86–96, jan 2013.
- [35] P. Keall, "4-Dimensional Computed Tomography Imaging and Treatment Planning," *Seminars in Radiation Oncology*, vol. 14, no. 1, pp. 81–90, 2004.
- [36] M. von Siebenthal, G. Székely, U. Gamper, P. Boesiger, A. Lomax, and P. Cattin, "4D MR imaging of respiratory organ motion and its variability," *Physics in Medicine and Biology*, vol. 52, no. 6, pp. 1547–1564, 2007.
- [37] B. Stemkens, R. H. Tijssen, B. D. de Senneville, H. D. Heerkens, M. van Vulpen, J. J. Lagendijk, and C. a.T. van den Berg, "Optimizing 4-Dimensional Magnetic Resonance Imaging Data Sampling for Respiratory Motion Analysis of Pancreatic Tumors," *International Journal of Radiation Oncology, Biology, Physics*, vol. 91, no. 3, pp. 571–578, 2015.
- [38] J. Cai, Z. Chang, Z. Wang, W. Paul Segars, and F.-F. Yin, "Four-dimensional magnetic resonance imaging (4D-MRI) using image-based respiratory surrogate: A feasibility study," *Medical Physics*, vol. 38, no. 12, p. 6384, 2011.
- [39] E. Tryggestad, A. Flammang, S. Han-Oh, R. Hales, J. Herman, T. McNutt, T. Roland, S. M. Shea, and J. Wong, "Respiration-based sorting of dynamic MRI to derive representative 4D-MRI for radiotherapy planning.," *Medical physics*, vol. 40, no. 5, p. 051909, 2013.
- [40] Y. Liu, F.-F. Yin, N.-k. Chen, M.-L. Chu, and J. Cai, "Four dimensional magnetic resonance imaging with retrospective k-space reordering: A feasibility study," *Medical Physics*, vol. 42, no. 2, pp. 534–541, 2015.
- [41] J. Yang, J. Cai, H. Wang, Z. Chang, B. G. Czito, M. R. Bashir, and F.-F. Yin, "Four-dimensional magnetic resonance imaging using axial body

- area as respiratory surrogate: initial patient results.," *International journal of radiation oncology, biology, physics*, vol. 88, pp. 907–12, mar 2014.
- [42] Y. Hu, S. D. Caruthers, D. A. Low, P. J. Parikh, and S. Mutic, "Respiratory amplitude guided 4-dimensional magnetic resonance imaging.," *International journal of radiation oncology, biology, physics*, vol. 86, pp. 198–204, may 2013.
- [43] D. Du, S. D. Caruthers, C. Glide-Hurst, D. A. Low, H. H. Li, S. Mutic, and Y. Hu, "High-quality t2-weighted 4-dimensional magnetic resonance imaging for radiation therapy applications.," *International journal of radiation oncology, biology, physics*, vol. 92, pp. 430–7, jun 2015.
- [44] W. Yang, Z. Fan, R. Tuli, Z. Deng, J. Pang, A. Wachsmann, R. Reznik, H. Sandler, D. Li, and B. A. Fraass, "Four-dimensional Magnetic Resonance Imaging with 3D Radial Sampling and Self-gating based K-space Sorting: Early Clinical Experience on Pancreatic Cancer Patients.," *International Journal of Radiation Oncology, Biology, Physics*, aug 2015.
- [45] Y. Liu, F.-F. Yin, B. G. Czito, M. R. Bashir, and J. Cai, "T2-weighted four dimensional magnetic resonance imaging with result-driven phase sorting.," *Medical physics*, vol. 42, pp. 4460–71, aug 2015.
- [46] Y. Yue, Z. Fan, W. Yang, J. Pang, Z. Deng, and E. McKenzie, "Geometric Validation of k-Space Self-gated 4D-MRI vs . 4D-CT Using a Respiratory Motion Phantom," vol. 5787, 2015.
- [47] N. Wink, C. Panknin, and T. D. Solberg, "Phase versus amplitude sorting of 4D-CT data.," *Journal of applied clinical medical physics / American College of Medical Physics*, vol. 7, pp. 77–85, jan 2006.
- [48] Y. Seppenwoolde, H. Shirato, K. Kitamura, S. Shimizu, M. van Herk, J. V. Lebesque, and K. Miyasaka, "Precise and real-time measurement of 3D tumor motion in lung due to breathing and heartbeat, measured during radiotherapy.," *International journal of radiation oncology, biology, physics*, vol. 53, pp. 822–34, jul 2002.
- [49] R. C. Gonzalez and R. E. Woods, *Digital Image Processing*. Pearson/Prentice Hall, 2008.
- [50] J. Sarker, A. Chu, K. Mui, J. A. Wolfgang, A. E. Hirsch, G. T. Y. Chen, and G. C. Sharp, "Variations in tumor size and position due to irregular breathing in 4D-CT: a simulation study.," *Medical physics*, vol. 37, pp. 1254–60, mar 2010.
- [51] H. Fayad, T. Pan, J. F. Clement, and D. Visvikis, "Technical note: Correlation of respiratory motion between external patient surface and internal anatomical landmarks.," *Medical physics*, vol. 38, pp. 3157–64, jun 2011.
- [52] D. P. Gierga, J. Brewer, G. C. Sharp, M. Betke, C. G. Willett, and G. T. Y. Chen, "The correlation between internal and external markers for abdominal tumors: implications for respiratory gating.," *International journal of radiation oncology, biology, physics*, vol. 61, pp. 1551–8, apr 2005.
- [53] K. Mori, H. Manabe, and K. Narikiyo, "Possible functional role of olfactory subsystems in monitoring inhalation and exhalation.," *Frontiers in neuroanatomy*, vol. 8, p. 107, jan 2014.

## Appendix

### A Manual

4D-MRI manual for Philips Ingenia 3T (Philips medical systems, Best) scanner using the Matlab program Tekelenburg4DMRI. The binning of the acquired images for a 4D-MRI dataset is not done automatically by the Philips Ingenia Scanner. This manual explains each step needed to acquire the 4D-MRI dataset. Because this program is a research version, the steps displayed herein should be closely followed and deviation of the protocol is probably not robust. A step by step explanation of each part of the program is done. Hopefully it will make it clear how the program is constructed to make it possible for adaptations and consequently improvement.

#### A.1 At the scanner

##### Pre-scanning preparation

To track respiratory motion a navigator is used. This navigator can be chosen as one of the sequence parameters at the 3T scanner. However, the navigator position should also be logged. This is not done automatically and should be done manually by activating it:

- Log in as gyrotest
- Open c:\temp\bstrace.dat
- Add the next line: mmurnav debug\_pos \*
- The scanner should be restarted by writing in a command window: "permproc stop scanner" followed by "permproc start scanner"

The navigator will now be logged in the logfile which can be found in:

- g:\log\devlogcurrent.log

Each navigator acquisition will be written to this file looking like:

- MMURNAV(debug\_pos): Pos.rel.to first nav = 15.01 mm, Max. Corr.=1.00

The devlogcurrent.log file should be obtained after scanning to make it possible to obtain the navigator derived respiratory trace.

##### Protocol parameters

The protocol used to acquire images can be selected at the scanner. Parameter optimization and even sequence choice is dependant on the user preference. To allow for 4D-MRI reconstruction the following parameters are important:

- The acquisition should be a 2D-acquisition or multi-2D acquisition (M2D)
- The navigator should be implemented by using the respiratory gating option (lead acquisition)
- The gating window should be sufficient to acquire continuously images (6 cm)

## A.2 4D-MRI reconstruction program

After image acquisition the devlogcurrent.log file is needed together with a directory containing all acquired MRI images. Sometimes the devlogcurrent.log file is very large. Selecting the logged data from your scan from the whole devlogcurrent.log file is necessary (and not implemented in the program). Select your performed scan by opening the logfile with a texteditor. Search for the part of the devlogcurrent.log file where your scan is logged.

The search for your scan in the very large devlogcurrent.log file can be accelerated by looking at the time stamp in the log file or by searching for the correct start of the scan by searching for "ReadyForScanSet".

Save your part of the devlogcurrent.log file in a separate textfile with a new name. Because the name of the logfile is used by the sorting algorithm it is beneficial to put the ID of your scan in the name of the textfile.

Your data is now ready for 4D-MRI reconstruction. Open the program Tekelenburg4DMRI in Matlab, see appendix B.1. Run the program by pressing the button 'Run' in the editor environment, see figure 1 or press F5.

### Acquisition parameter input

The first part of the program consists of a couple of questions concerning parameter input. The input needed are the number of slices and the number of dynamics used at image acquisition. The questions are asked in the command window and can be answered in the same window by typing a number and pressing 'enter', see figure 1.

### Select log file

After the 3 questions a dialog box opens with the title '**Select log file of your scan for navigator extraction**', as shown in figure 2. Go to your saved logfile containing the navigator data and double click on this file.

Next, another question requires input in the command window : '**Is the data interleaved? Input yes or no:**'. Input yes if the data is acquired in interleaved submode, input no if the slices are acquired contiguous.

Another dialog box with the title '**Choose directory with raw images from image acquisition**' appears. Go to the directory with the acquired MR images and double click on this directory.

This dialog box is followed with an dialog box with the title: '**Choose the folder for the 4D-MRI binning of the ampli method**'. Choose a folder where you would like the amplitude binning result to be saved.

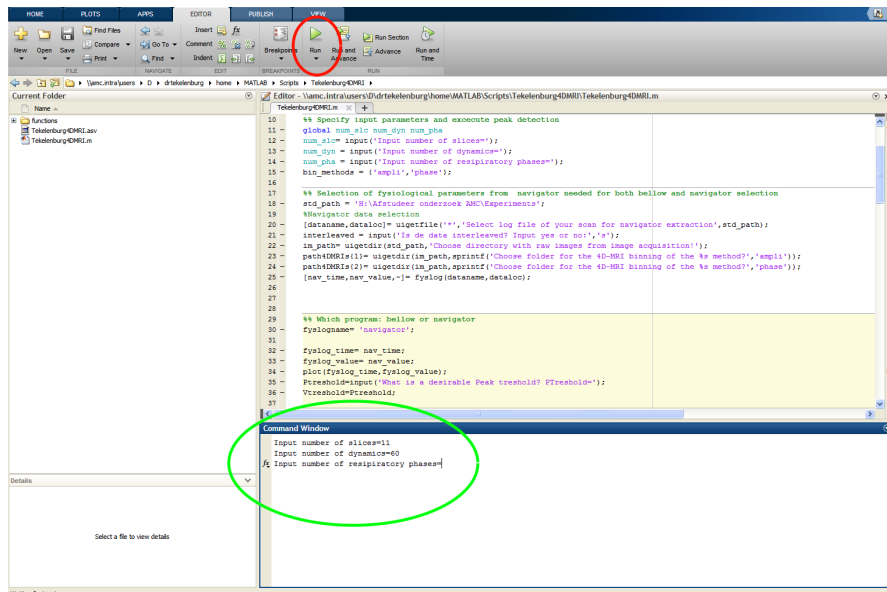


**Figure 1:** The start of the program Tekelenburg4DMRI.m. The 'Run' button is displayed (red) and an example is given in the command window where parameter input is required (green).

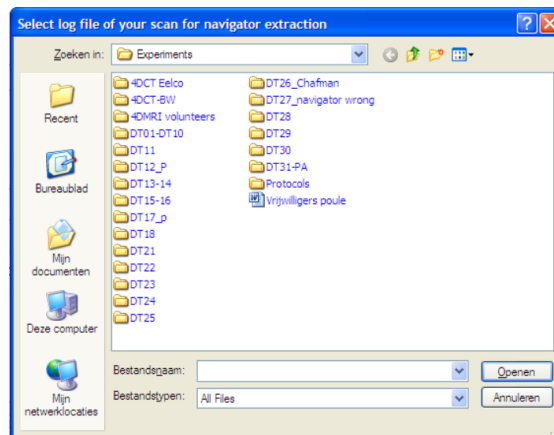


**Figure 2:** Dialog box that asks for the selection of the logfile containing navigator data.

The last dialog box is the one with the dialog box for the selection of the folder for phase binning with the title :'**Choose the folder for the 4D-MRI binning of the phase binning method**'.

### Navigator extraction and Binning

When the correct folders and the logfile are selected, the program runs the function `fyslog` (see appendix B.2).

This program extracts the navigator acquisition from your logfile and returns arrays with the navigator value and navigator time stamp.

The navigator is measured relative to the first acquired navigator. An artificial baseline has to be determined to assist the peak detection algorithm. To improve this a number corresponding to a horizontal line should be determined. Therefore, a plot of the navigator trace is displayed when the `fyslog` is executed correctly.

My advice is to try to select a number that allows to differentiate between end-exhale and inhale positions. The number you input will be chosen as baseline and all values above this number will be treated as peaks while the values below will be treated as troughs. Be aware of variations in peaks and troughs and choose the number accordingly.

A single number is needed as input which corresponds to a horizontal line in the plot : **"Choose base line for peak detection, input a number : "**.

After selecting an appropriate number, the program will run the functions `PhaseBin_onlynav.m`, `AmpliBin_onlynav.m` and `binImages`, see appendix B.3. `PhaseBin_onlynav.m` and `AmpliBin_onlynav.m` extracts the required bins from the navigator data.

`Bin_images` is the most important result from these functions. This variable contains for each slice and dynamic the assigned bin.

The variable `bin_images` is used by the function `binImages` to sort the actual images into its corresponding bin. The process of binning can take a couple of minutes and after binning a slice is displayed. This slice is needed to select the diaphragm for median selection.

### **Median selection**

The median image from the redundant data set is selected by the function `Select-median.m`, see appendix B.4. This function requires the diaphragm of the image and this is acquired using a clip-box (already automatically created). To select the diaphragm draw a square using the computer mouse selecting the diaphragm (do not include parts of the bronchus, heart or ribcage), see figure 3a. When satisfied with the clip-box, double click inside this box.

This process continues until all diaphragm positions for each slice are selected. Then the program will select the median image. A waiting bar shows the progress of this selection process. After median selection the program will ask for one more diaphragm position. This clip-box is needed for diaphragm discontinuity analysis. It is important to use a relatively thin and long clip-box as shown in figure 3b. The reason for this is the anatomy of the diaphragm, as it is not registered to the same slice position but over the whole volume. There is a minimum width of the clip-box, the shape of the clip-box changes when the clip-box is chosen too thin, see figure 3. Double click after selection of the diaphragm. The clip-box positions are saved as matlab workspace using the name of the logfile with an added `'pos_tocrop'`.

All cropped image are rigidly registered to a reference image using the function `'rigidReg.m'`, see appendix B.5.

The correct 4D-MRI dataset is obtained after the median selection and saved in the selected folders in the directory `'Median selected 4D-MRI'`.

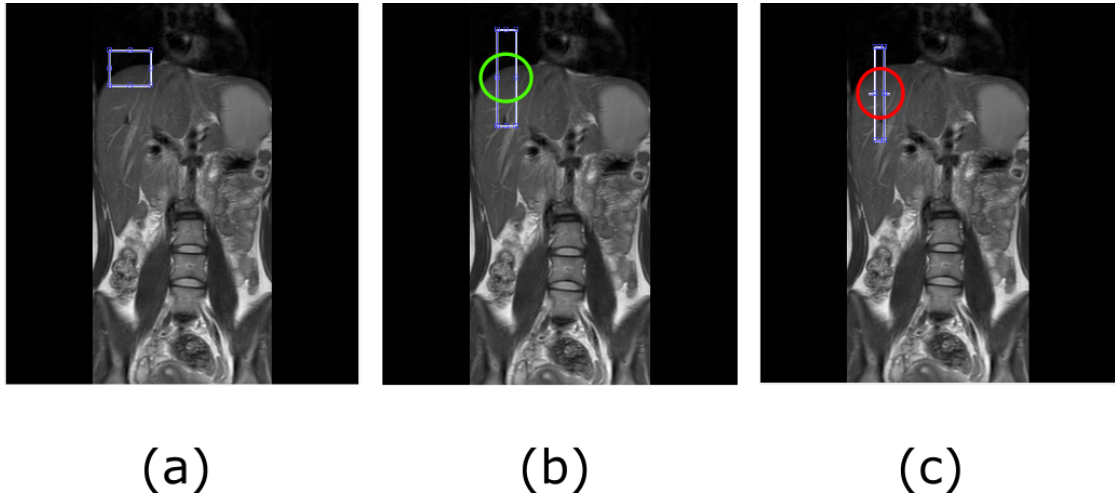


**Figure 3:** Clipbox for selection of the diaphragm. An example for an clip-box by selecting the diaphragm for median selection (a). The clipbox for diaphragm discontinuities should be thin and large (b). If the clipbox is smaller than allowed it is revealed by the shape of the clipbox(c). The red and green circles show the place where the clipbox changes shape when a wrong size is chosen.

Finally, the program selects from each bin the the same slice and adds them in the directory 'respiratory signal' using the function 'StackAndGif.m', see appendix B.6. It also creates a GIF movie for each slice position and this gif is displayed and stored.

#### Analysis functions

The final step is the function `Comparemethods.m`, this function calculates the respiratory signal for each method. This function together with `calcOrganDiscontinuity.m` and `SpreadCal.m` collect data that could be useful for analysis, see appendix B.6. All this data is stored in a Matlab workspace using the name of the navigator logfile preceded by 'workspace\_'.

Potentially useful variables are:

- **binning\_images:** Assigned bin to each slice positions and dynamic
- **dataCompl:** the data completeness for both methods (%)
- **spread:** the variation of the diaphragm position per bin and slice position
- **stde:** the standard deviation of the values in spread
- **max\_spread:** the largest stde for all slice and bin positions for each method
- **diamovement:** the diaphragm motion for each slice is shown (mm)
- **bins:** the used bins for each slice position is are stored in this variable
- **continuity\_dia:** the diaphragm shape for each bin

## B Program

### B.1 Tekelenburg4DMRI.m

The main program that calls all the needed functions for 4D-MRI reconstruction.

```
1 %% 4D-MRI total extraction
2 clear all
3 close all
4 clc
5
6 %%
7 a=cd;
8 addpath(fullfile(a, 'functions'));
9
10 %% Specify input parameters and execute peak detection
11 global num_slc num_dyn num pha
12 num_slc= input('Input number of slices=');
13 num_dyn = input('Input number of dynamics=');
14 num pha = input('Input number of respiratory phases=');
15 bin_methods = {'ampli', 'phase'};
16
17 %% Selection of physiological parameters from navigator needed for ...
    both bellow and navigator selection
18 std_path = 'H:\Afstudeer onderzoek AMC\Experiments';
19 %Navigator data selection
20 [dataname, dataloc]= uigetfile('*', 'Select log file of your scan for ...
    navigator extraction', std_path);
21 interleaved = input('Is de data interleaved? Input yes or no:', 's');
22 im_path= uigetdir(std_path, 'Choose directory with raw images from ...
    image acquisition!');
23 path4DMRIs{1}= uigetdir(im_path, sprintf('Choose folder for the 4D-MRI ...
    binning of the %s method?', 'ampli'));
24 path4DMRIs{2}= uigetdir(im_path, sprintf('Choose folder for the 4D-MRI ...
    binning of the %s method?', 'phase'));
25 [nav_time, nav_value, ~]= fyslog(dataname, dataloc);
26
27
28
29 %% Navigator
30 fyslogname= 'navigator';
31
32 fyslog_time= nav_time;
33 fyslog_value= nav_value;
34 plot(fyslog_time, fyslog_value);
35 Pthreshold=input('Choose base line for peak detection, input a number: ');
36 Vthreshold=Pthreshold;
37
38 %% Bin phase and amplitude automatically
39
40 for bm=1:length(bin_methods)
```

```

41     bin_method= bin_methods{bm};
42 %% Peak detection, Phase and Amplitude binning
43
44
45 if strcmp('phase',bin_method)==1
46
47     [bin_images,nav_posImages,peakvaly_time,peakvaly_val] = ...
48         PhaseBin_onlynav(fyslog_value,...
49             fyslog_time,Ptreshold,interleaved);
49     navigator_index.phase=nav_posImages;
50     binning_images.phase=bin_images;
51 elseif strcmp('ampli',bin_method)==1
52
53
54
55     [bin_images,nav_posImages,peakvaly_time,peakvaly_val,peak_avg,valy_avg] ...
56         = AmpliBin_onlynav(fyslog_value,...
57             fyslog_time,Ptreshold,Vtreshold,interleaved);
57     navigator_index.ampli= nav_posImages;
58     binning_images.ampli=bin_images;
59 else
60     error('Did not choose correct binning method, choose ampli or phase')
61 end
62
63
64
65 %%
66 hold off
67
68 %% Load images and bin in correct folder
69 % Choose path for image acquisition and feed to extract DICOM
70
71 binImages(im_path,...
72 path4DMRIs{bm},bin_images,nav_posImages,dataname,bin_method);
73
74 %% Make an MRI (either simple or Average) & slice selection& GIF
75 pos_tocropfile= [dataname(1:end-4) '_pos_tocrop.mat'];
76 if exist(pos_tocropfile,'file')==2
77     load(pos_tocropfile,'pos_tocrop')
78     [avg_save_path,pos_tocrop,spread_avg]= ...
79         Selectmedian(path4DMRIs{bm},fyslogname,pos_tocrop);
80     [disc_dia,pos_tocrop]= ...
81         calcOrganDiscontinuity(avg_save_path,pos_tocrop);
82 else
83     pos_tocrop= cell(num_slc+2,1);
84     [avg_save_path,pos_tocrop,spread_avg]= ...
85         Selectmedian(path4DMRIs{bm},fyslogname,pos_tocrop);
86     [disc_dia,pos_tocrop]= ...
87         calcOrganDiscontinuity(avg_save_path,pos_tocrop);
88     save(pos_tocropfile,'pos_tocrop')
89 end

```

```

86
87 [perci_maxvalue,maxi_spread,std_spread]= SpreadCal (spread_avg);
88
89 if strcmp(bin_method,'ampli')
90     continuity_dia.ampli= disc_dia;
91     spread.ampli= spread_avg;
92     perc_mvalue.ampli=perci_maxvalue;
93     max_spread.ampli= maxi_spread;
94     stde.ampli = std_spread;
95 elseif strcmp(bin_method,'phase')
96     continuity_dia.phase=disc_dia;
97     spread.phase = spread_avg;
98     perc_mvalue.phase=perci_maxvalue;
99     max_spread.phase=maxi_spread;
100    stde.phase= std_spread;
101 end
102
103 %[avg_save_path]= CreateSimple4DMRI (path4DMRI);
104
105 %% Make
106 respiratory_dirname= 'Respiratorysignal';
107 mkdir (avg_save_path,respiratory_dirname);
108
109 slc_save_path=cell (num_slc,1);
110 for i= 1:num_slc
111     slc_save_path{i}=StackAndGif (avg_save_path,i,dataname);
112 end
113
114 end
115 %% Compare methods Ampli, phase
116
117 [diamovement,bins,pos_tocrop]= ...
    CompareMethods (path4DMRIs{1},path4DMRIs{2},pos_tocrop);
118
119
120 %% Data completeness
121
122 for i = 1: num_slc
123     missing_pbin(i).ampli= length(diamovement.ampli(i).avg);
124     missing_pbin(i).phase= length(diamovement.phase(i).avg);
125 end
126
127 dataCompl.ampli= sum([missing_pbin.ampli])/ (num_pha*num_slc);
128 dataCompl.phase= sum([missing_pbin.phase])/ (num_pha*num_slc);
129
130 %% Save data as matlab workspace
131
132 save(['workspace_' dataname(1:end-4)]);

```

## B.2 `fyslog.m`

Extraction of navigator data from a logfile.

```
1 function [time_s,navigator,dynamictime_s]= fyslog(dataname,dataloc)
2
3
4
5 %% Create search strings and position of corresponding value string
6 search_nav= 'MMURNAV(debug_pos):';
7 search_dyn = 'Performing';
8 search_fin = 'Finalize';
9 %location of the corresponding string
10 timestring= 7;
11 navstring= 7;
12 dyntimestring= 13;
13 finstring= 3;
14
15
16 %% Find location navigatorvalue and timestamp
17
18 fileID= fopen([dataloc dataname]);
19 text = textscan(fileID,'%s');
20 fclose(fileID);
21
22 loc_nav= find(strcmp(text{1},search_nav));
23 loc_dyn=find(strcmp(text{1},search_dyn));
24 loc_fin= find(strcmp(text{1},search_fin));
25 for i = 1:length(loc_nav)
26     timecell{i}= text{1}(loc_nav(i)-timestring);
27     navcell{i}=text{1}(loc_nav(i)+navstring);
28 end
29
30 for i = 1:length(loc_dyn)
31     %check if search_dyn did not encounter the wrong (but the same string)
32     if strcmp(text{1}(loc_dyn(i)+1),'dynamic')== 1;
33         dyncell{i}= text{1}(loc_dyn(i)-dyntimestring);
34     end
35 end
36 dyncell{end+1}= text{1}(loc_fin-finstring);
37
38
39
40 %% Process to get plottable data
41 time_dyn = char([dyncell{:}]);
42 time_pos = char([timecell{:}]);
43 nav_pos = char([navcell{:}]);
44
45 % Hier haal ik de : punt weg
46 time_pos= [time_pos(:,1:2), time_pos(:,4:5), time_pos(:,7:end)];
47 time_dyn= [time_dyn(:,1:2), time_dyn(:,4:5), time_dyn(:,7:end)];
```

```

48
49 for i = 1:length(loc_nav)
50     navigator(i) = str2double(nav_pos(i,:));
51     time(i)= str2double(time_pos(i,:));
52 end
53
54 for i = 1:length(time_dyn)
55     dynamictime(i)= str2double(time_dyn(i,:));
56 end
57
58 % calculate timestamp
59 h= fix(time/10000);
60 h1= fix(dynamictime/10000);
61
62 tot_min= (time/10000-h)*100;
63 m= fix(tot_min);
64 m2= fix((dynamictime/10000-h1)*100);
65
66 s= (tot_min-m)*100;
67 s2= (dynamictime/100-fix(dynamictime/100))*100;
68
69 %Ovoid the wrong rounding
70 cor_m= s>=60;
71 s(cor_m)=0;
72 m=m+cor_m;
73 time_s= h*60*60+ m*60+s;
74 dynamictime_s= h1*60*60+ m2*60+s2;
75 %% Calculate average frequency of navigator
76 f_nav= length(navigator)/max(time_s);
77
78
79
80 %Correction for drift in the set of, set set of around 0
81 nav_drift= (max(navigator)+min(navigator))/2;
82 navigator= navigator - nav_drift;
83
84 time_s= time_s - time_s(1);
85 dynamictime_s= dynamictime_s- dynamictime_s(1);
86
87
88
89
90
91 end

```

## B.3 Binning

### B.3.1 AmpliBin\_onlynav.m

```

1
2 function [bin_images_t,nav_posImages,peakvaly_time,peakvaly_val,peak_avg,valy_avg,valy_media
   ...
3     AmpliBin_onlynav(fyslog_value, ...
        fyslog_time,Ptreshold,Vtreshold,interleaved)
4
5 global num_dyn num_slc num pha
6 %% find peaks and valleys
7 peak_log = imregionalmax(fyslog_value);
8 valy_log = imregionalmin(fyslog_value);
9
10 %Eerst de posities behouden van peak_time, later pas echte tijd stamp ...
    geven
11 peak_pos = find(peak_log);
12 peak_val= fyslog_value(peak_log);
13
14 %Eerst de posities behouden van valy_time, later pas echte tijd stamp ...
    geven
15 valy_pos = find(valy_log);
16 valy_val= fyslog_value(valy_log);
17
18 %% Remove wrong values and double peak and valley detections
19
20 Pdouble_pos=[];
21
22 peak_pos(peak_val<Ptreshold)= [];
23 peak_val(peak_val<Ptreshold)= [];
24
25
26 Vdouble_pos=[];
27
28 valy_pos(valy_val>Vtreshold)= [];
29 valy_val(valy_val>Vtreshold)= [];
30
31
32 %Stil needed the indices from the peaks
33 for i= 1:length(peak_val)-1
34     p_nav= fyslog_value(peak_pos(i):peak_pos(i+1));
35     p_nav =all(p_nav > Ptreshold);
36
37     if p_nav == 1
38         %als er twee peaks zijn(verkeerde en dus geen dal is) neem ...
            gemiddelde
39         peak_pos(i:i+1) = round ((peak_pos(i+1)+peak_pos(i)) / 2);
40         peak_val(i:i+1) = max([peak_val(i+1),peak_val(i)]);
41         Pdouble_pos(end+1)= i;
42     end
43     if p_nav == 0
44         peak_pos(i) = peak_pos(i);
45         peak_val(i) = peak_val(i);
46     end

```

```

47 end
48
49 for i= 1: length(valy_val)-1
50
51     v_nav= fyslog_value (valy_pos (i):valy_pos (i+1));
52     v_nav =all(v_nav < Vtreshold);
53
54     if v_nav == 1
55         %als er twee dalen zijn(verkeerde en dus geen piek) zit neem ...
56         %gemiddelde
57         valy_pos(i:i+1) = round ((valy_pos(i+1)+valy_pos(i)) / 2);
58         valy_val(i:i+1) = min([valy_val(i+1),valy_val(i)]);
59         Vdouble_pos(end+1)= i;
60     end
61     if v_nav == 0
62         valy_pos(i) = valy_pos(i);
63         valy_val(i) = valy_val(i);
64     end
65 end
66 peak_pos (Pdouble_pos)= [];
67 peak_val (Pdouble_pos)=[];
68
69 valy_pos (Vdouble_pos)=[];
70 valy_val (Vdouble_pos)=[];
71
72 %Return the time positions to the fysical time stamps.
73 peak_time= fyslog_time (peak_pos);
74 valy_time= fyslog_time (valy_pos);
75
76 %% Make bins for every breathing phase via amplitude binning
77 num_couples= num pha/2;
78
79 peak_avg= mean(peak_val);
80 % peak_median=median(peak_val);
81 % peak_modus= mode(round(peak_val*4)/4);
82
83 valy_avg = mean(valy_val);
84 % valy_median= median(valy_val);
85 % valy_modus= mode(round(valy_val*4)/4);
86 % Give each navigator time a bin in the form of a couple.
87 couple_amp= abs(peak_avg-valy_avg)/num_couples;
88 couple_bin= peak_avg;
89
90 for i= 1:num_couples
91     couple_bin(end+1)= peak_avg- i*couple_amp;
92 end
93 couple_bins= zeros(1,length(fyslog_time));
94 navigator_bins= zeros(1,length(fyslog_time));
95
96 for i= 1:length(fyslog_value)

```

```

97     for b= 1:num_couples
98         if fyslog_value(i)< couple_bin(b) && fyslog_value(i)> ...
99             couple_bin(b+1);
100            couple_bins(i)= b;
101        end
102    end
103
104    %% Plotting commands
105
106
107    % plot(fyslog_time,fyslog_value);
108    % %Plot merge peak and valeys
109    % hold on
110    % scatter(peak_time,peak_val);
111    % scatter(valy_time,valy_val);
112
113    %% Couple_diff is not robust due to noise on the diff(nav_value) use ...
114    peak&valy:
115    %Merge peak and valley to extract the sign of the slope for couple
116    %de-coupling
117
118
119    peakvaly_time= [];
120    %If valy and peaks have the same length
121    if length(valy_val)== length(peak_val)
122        if peak_time(1)> valy_time(1) %When there is first a valley
123            peakvaly_val= kron(valy_val,[1 0])+ kron(peak_val,[0 1]) ;
124            peakvaly_time= kron (valy_time,[1 0]) + kron(peak_time,[0 1]);
125        else % When there is first a peak
126            peakvaly_val = kron(peak_val,[1 0]) + kron(valy_val,[0 1]);
127            peakvaly_time = kron(peak_time, [1 0])+ kron(valy_time, [0 1]);
128
129        end
130        %If there are less valeys than peaks
131    elseif length(valy_val) < length(peak_val)
132        dummyspeak_val= peak_val(1:end-1);
133        dummyspeak_time= peak_time(1:end-1);
134        peakvaly_val = kron(dummyspeak_val,[1 0]) + kron(valy_val,[0 1]);
135        peakvaly_time = kron(dummyspeak_time, [1 0])+ kron(valy_time, [0 1]);
136        %append redundant peak
137        peakvaly_val(end+1)= peak_val(end);
138        peakvaly_time(end+1)= peak_time(end);
139        % if there are less peaks than valleys
140    elseif length(valy_val) > length(peak_val)
141        dummyvaly_val = valy_val(1:end-1);
142        dummyvaly_time= valy_time(1:end-1);
143        peakvaly_val= kron(dummyvaly_val,[1 0])+ kron(peak_val,[0 1]) ;
144        peakvaly_time= kron (dummyvaly_time,[1 0]) + kron(peak_time,[0 1]);
145

```

```

146     %append redundant valy
147     peakvaly_val(end+1)= valy_val(end);
148     peakvaly_time(end+1)= peak_time(end);
149 end
150
151 %% Plot peakvalley time
152
153 % figure(2)
154 % plot(fyslog_time,fyslog_value);
155 % %Plot merge peak and valeys
156 % hold on
157 % scatter(peakvaly_time,peakvaly_val)
158
159
160 %% Create slope array (peakvalybin_slope) for each navigator point ...
    using peakvaly_val
161
162 peakvaly_slope= diff(peakvaly_val);
163
164 peakvalybin_slope= [];
165 % For each navigator time stamp give it a slope value
166 for i= 1: length(fyslog_time)
167     %First the difference between time 0 and the first peak/valey.
168     if fyslog_time(i)≥0 && fyslog_time(i)<peakvaly_time(1)
169         peakvalybin_slope(end+1)= -peakvaly_slope(1);
170     end
171     for s=1: length(peakvaly_time)-1
172         %For each peak in between
173         if fyslog_time(i)≥ peakvaly_time(s) && fyslog_time(i)< ...
            peakvaly_time(s+1)
174             peakvalybin_slope(end+1)= peakvaly_slope(s);
175         end
176     end
177     %Last the difference between last peak/valey and end
178     if fyslog_time(i) > peakvaly_time(end)
179         peakvalybin_slope(end+1)= -peakvaly_slope(end);
180     elseif fyslog_time(i) == peakvaly_time(end)
181         peakvalybin_slope(end+1)= peakvaly_slope(end);
182     end
183
184
185 end
186
187
188
189 %% Use peakvalybin_slope to decouple each couple to obtain correct BIN ...
    value per navigator time stamp.
190 %Possible to change the binning to obtain
191
192 for i = 1: length(couple_bins)
193     if peakvalybin_slope(i) > 0

```

```

194     if couple_bins(i) == 1
195         couple_bins(i) = 10;
196     elseif couple_bins(i) == 2
197         couple_bins(i) = 9;
198     elseif couple_bins(i) == 3
199         couple_bins(i) = 8;
200     elseif couple_bins(i) == 4
201         couple_bins(i) = 7;
202     elseif couple_bins(i) == 5
203         couple_bins(i) = 6;
204     end
205 end
206 end
207
208
209 %% Correct for interleaved acquisition
210 ar_slice=1:num_slc;
211 start_serie= 2;
212 if strcmp('yes',interleaved)==1
213     i_step= round(sqrt(num_slc));
214     for i=2:num_slc
215         ar_slice(i)= ar_slice(i-1)+i_step;
216         if ar_slice(i)>num_slc
217             ar_slice(i)= start_serie;
218             start_serie= start_serie+1;
219         end
220     end
221 end
222
223 %% Sort images with only using navigator in corresponding bin and ...
224     return bin_images_t
225 bin_images_t= zeros(num_dyn,num_slc);
226 nav_posImages= zeros(num_dyn,num_slc);
227
228 dyn1_remove= length(fyslog_value) - (num_slc*(num_dyn-1));
229 fyslog_val_nod1= fyslog_value(dyn1_remove+1:end);
230 for i=1:length(fyslog_val_nod1)
231     %%Watch this carefully, should work though (transposed and reversed ...
232     s,d)
233     [s,d]= ind2sub(size(bin_images_t'),i);
234     %%d+1 because the first dynamic should be noticed and skipped
235     bin_images_t(d+1,ar_slice(s))= couple_bins(dyn1_remove+i);
236     nav_posImages(d+1,ar_slice(s))= dyn1_remove+i;
237 end

```

### B.3.2 PhaseBin\_onlynav.m

```

1 %% detected peak with findpeak func and peak_time
2

```

```

3 function [im_phase,nav_posImages,peak_time,peak_val] = ...
    PhaseBin_onlynav(fyslogdata,time_s,treshold,interleaved)
4 global num_dyn num_slc num pha
5 %% find peaks
6 peak_log = imregionalmax(fyslogdata);
7 peak_pos = find(peak_log);
8 peak_val= fyslogdata(peak_log);
9
10
11
12 %% Remove negative values and double peak detections
13 double_pos=[];
14 peak_pos(peak_val<treshold)= [];
15 peak_val(peak_val<treshold)= [];
16
17 for i= 1:length(peak_val)-1
18     p_nav= fyslogdata(peak_pos(i):peak_pos(i+1));
19     p_nav =all(p_nav > treshold);
20     if p_nav == 1
21         %als er twee (verkeerde en dus dezelfde) peaks zijn neem ...
            gemiddelde
22         peak_pos(i:i+1) = round ((peak_pos(i+1)+peak_pos(i)) / 2);
23         peak_val(i:i+1) = max([peak_val(i+1),peak_val(i)]);
24         double_pos(end+1)= i;
25     end
26     if p_nav == 0
27         peak_pos(i) = peak_pos(i);
28         peak_val(i) = peak_val(i);
29     end
30 end
31 peak_pos(double_pos)= [];
32 peak_val(double_pos)=[];
33 peak_time= time_s(peak_pos);
34
35
36
37
38 %% Give time stamp to each dicom image
39
40
41 % Make bins for every breathing phase by extracting cycle time
42 peak_time2=[peak_time(2:end) 0];
43
44 resp_cycle_time = abs(peak_time(1:end-1) - peak_time2(1:end-1));
45
46 phase_time = resp_cycle_time / num pha ;
47 dyn1_remove= length(time_s) - (num_slc*(num_dyn-1));
48 fyslog_val_nod1= time_s(dyn1_remove+1:end)';
49 %Sort images per to return time per image.
50
51 total_imagetimestamp = reshape(fyslog_val_nod1,[num_slc,num_dyn-1])';

```

```

52
53
54
55 %% Counter interleaved acquisition
56 ar_slice=1:num_slc;
57 start_serie= 2;
58 if strcmp('yes',interleaved)==1
59     i_step= round(sqrt(num_slc));
60     for i=2:num_slc
61         ar_slice(i)= ar_slice(i-1)+i_step;
62         if ar_slice(i)>num_slc
63             ar_slice(i)= start_serie;
64             start_serie= start_serie+1;
65         end
66     end
67 end
68
69 %% Sort images in corresponding phase bin
70 %This is implemented to sort bin 1 and bin 10 evenly
71 sortbin= 1;
72 nav_posImages=zeros(num_dyn, num_slc);
73 im_phase= zeros(num_dyn, num_slc);
74 for s= 1: num_slc
75     for d = 1: num_dyn-1
76
77         im_timestamp = total_imagetimestamp(d,s);
78         %This is to extract the navigator:
79         [~,index]= min(abs(time_s-im_timestamp));
80         nav_posImages(d+1,ar_slice(s))= index;
81
82         for i= 1: length(peak_time)-1
83             if im_timestamp==peak_time(i)
84                 if mod(sortbin,2)== 0
85                     im_phase(d+1,ar_slice(s))= 1;
86                     sortbin= sortbin +1;
87                 else
88                     im_phase(d+1,ar_slice(s))= 10;
89                     sortbin= sortbin+1;
90                 end
91             end
92
93
94
95             if im_timestamp > peak_time(i) && im_timestamp < ...
96                 peak_time(i+1)
97                 for p=1: num pha
98                     if im_timestamp < peak_time(i)+ phase_time(i)*p
99                         im_phase(d+1,ar_slice(s))= p;
100                         break
101                     end
102                 end
103             end
104         end
105     end
106 end

```

```

102         end
103     end
104 end
105
106 end
107
108
109 end

```

### B.3.3 binImages.m

```

1  %%% Upload images from directory and store them in X
2  function [path1] = ...
3      binImages(impath,path1,bin_images,Nav_posimages,dataname,bin_method)
4
5  %% Save corresponding images in bin
6  %path1= uigetdir(impath,sprintf('Choose folder for the 4D-MRI binning ...
7      of the %s method?',bin_method));
8
9  %%make folders and series ID for each respiratory phase serie
10 for i= 0:num pha
11     mkdir(path1,num2str(i))
12     delete_content_binpath= fullfile(path1,num2str(i),'*');
13     delete(delete_content_binpath);
14     serie_id{i+1}= dicomuid;
15 end
16
17 %% Read Dicom files and create image location X
18 imfiles= fullfile(impath,'*.dcm');
19 imstot=dir(imfiles);
20
21
22 %Fill X with corresponding images and send them to corresponding bin
23 for i=1:length(imstot)
24     %h=waitbar(i/length(imstot),'Percentage of of images binned');
25     %Read images
26     filename = fullfile(impath,imstot(i).name);
27     X= dicomread(filename);
28     metadata= dicominfo(filename);
29     %Write each image to corresponding bin
30     [d,s] = ind2sub(size(bin_images),i);
31     bin = bin_images(i);
32     %Dit moet ik nog veranderen naar iets beters
33     metadata.StudyID(6)= num2str(7);
34     %%%%%%%%%%%%%%%%%%%%%%%%%%%%%%%%%%%%%%%%%%%%%%%%%%%%%%%%%%%%%%%%%%%%%%%%%
35     metadata.NumberOfTemporalPositions= num pha;
36     metadata.NavigatorIndex = Nav_posimages (i);

```

```

37     metadata.TemporalPositionIdentifier= bin;
38     metadata.SeriesInstanceUID = serie_id{bin_images(i)+1};
39     metadata.SeriesDescription = ...
        sprintf('%s_%0.3dbin_%s_%s', dataname(1:8), bin, bin_method, dataname(13:15));
40     im_name=sprintf('slice%04d_dyn%04d_%s', s, d, imstot(i).name);
41     bin_path= fullfile(path1, num2str(bin), im_name);
42     dicomwrite(X, bin_path, 'CreateMode', 'Copy', metadata);
43     %close(h)
44 end

```

## B.4 Selectmedian.m

```

1 function ...
    [simple_save_path, pos_tocrop, spread_inBin]=Selectmedian(impath, fyslogname, pos_tocrop)
2
3 global num pha num_slc
4
5 %% Create Average images
6 simple_string= sprintf('Median selected 4D-MRI');
7 simple_save_path = fullfile(impath, simple_string);
8
9 %% Average in each bin the same slices to create
10
11 bins=1:num pha;
12 slices= 1:num_slc;
13 X=uint16([]);
14 spread_inBin= cell(num pha, num_slc);
15 for b= bins
16     h=waitbar(b/num pha, 'Percentage of bins completed by median ...
        selection:');
17     mkdir(simple_save_path, num2str(b));
18     bin_save_path= fullfile(simple_save_path, num2str(b));
19     filename = fullfile(impath, num2str(b));
20     imfiles= fullfile(impath, num2str(b), '*.dcm');
21     delete_content_save_path= fullfile(bin_save_path, '*');
22     delete(delete_content_save_path);
23     imstot = dir(imfiles);
24     for s=slices
25         num_imag=1;
26
27         for im= 1: length(imstot)
28             % Check for dyn=1 -> and rename to not be used
29             if str2double(imstot(im).name(14:17)) == 1
30                 imstot(im).name(8:9)=0;
31             end
32             if str2double(imstot(im).name(6:9))==s
33                 im_name= fullfile(filename, imstot(im).name);
34                 X(:, :, num_imag)= dicomread(im_name);
35                 num_imag=num_imag+1;

```

```

36         metadata= dicominfo(im_name);
37         im_correct= im;
38     end
39 end
40
41     %Check if the slice was present in the bin
42     if isempty(X)==1
43         continue
44     end
45     %Check if position of diafragma crop is present
46     if isempty(pos_tocrop{s})==1
47         [r,pos_tocrop{s}]= imcrop(X(:,:,1),[]);
48         close all
49     end
50     %pos_tocrop for discontinuity
51
52     %     if isempty(pos_tocrop{num_slc+2})==1
53     %         msgbox('Select diaphragm for discontinuity analysis, ...
press enter (twice)')
54     %         pause()
55     %         [r,pos_tocrop{num_slc+2}]= imcrop(X(:,:,1),[]);
56     %     end
57
58
59
60     dia_movement=rigidReg('change func rigidReg',X,pos_tocrop{s});
61     spread_inBin{b,s}= dia_movement;
62     %Find best diamovement value WHILE countering evenly ...
distributed values
63     [r,r,ZZ]= size(X);
64     X_outrange=1:ZZ;
65     dia_counter=0;
66     dia_median= median(dia_movement);
67     while length(X_outrange)== ZZ
68         X_outrange=[];
69         dia_median_range= ...
[diagonal_median-dia_counter,diagonal_median+dia_counter];
70     for i= 1:length(dia_movement)
71         dia_poschek= dia_movement(i)> dia_median_range;
72         if dia_poschek(1)==1 && dia_poschek(2)==0
73             continue
74         else
75             X_outrange(end+1)=i;
76         end
77     end
78
79     dia_counter= dia_counter+0.1;
80 end
81
82 X(:,:,X_outrange)=[];

```

```

83     %This can be improved using the best suitable solution or ...
84     something
85     avg=X(:,:,1);
86     [r,r,ZZ]= size(avg);
87     imavgsav_name= ...
88         sprintf('slice%0.4d_bin%0.4d_%s_Average%0.2d',s,b,fyslogname,ZZ);
89     imsav_name= ...
90         sprintf('%s%s',imavgsav_name,imstot(im_correct).name(end-3:end));
91     bin_path=fullfile(bin_save_path,imsav_name);
92     %metadata.SeriesDescription = 's',namesequence, bin,;
93     dicomwrite(avg,bin_path,'CreateMode','Copy',metadata);
94     X=uint16([]);
95 end
96 close(h)
97 end
98
99 end

```

## B.5 Rigid registration program

```

1 %% Extract diaphragm and in the future pancreatic motion from 4DMRI
2 function [dia_movement]= rigidReg(slc_save_path,X,pos)
3 close all
4
5 global num_slc
6 cd('H:\MATLAB');
7 addpath('H:\MATLAB\Scripts');
8 [opti,metric]=imregconfig('monomodal');
9
10
11 %% Apply rigid registration
12
13
14 switch nargin
15     case 1
16         imfiles= fullfile(slc_save_path,'*.dcm');
17         imstot = dir(imfiles);
18         X=uint16([]);
19         for i= 1:length(imstot)
20             im4DMRI= fullfile(slc_save_path,imstot(i).name);
21             X(:,:,i)= dicomread(im4DMRI);
22         end
23         h=msgbox('Select Diaphragm');
24         pause(0.2)
25         [im_diafrag, pos]=imcrop(X(:,:,1),[]);
26         close(h)

```

```

27         close all
28
29         case 3
30             clear slc_sav_path
31             [im_diafrag, pos]= imcrop(X(:,:,1),pos);
32         end
33
34         [r,r,ZZ]= size(X);
35         %Preallocation of X_crop
36         [imx,imy]= size(im_diafrag);
37         X_crop = repmat(uint16(0), [imx imy ZZ]);
38
39         for i=1:ZZ
40             X_crop(:,:,i) = imcrop(X(:,:,i),pos);
41             se=strel('disk', 2);
42             im= X_crop(:,:,i)>25;
43             im= bwareaopen(im,150);
44             X_crop(:,:,i)=imclose(im,se);
45         end
46
47
48         %% Apply registration method (intensity based)
49
50         strt_im= X_crop(:,:,1);
51
52         for i=1:ZZ
53             crop_transformation = ...
54                 imregtform(strt_im+0,X_crop(:,:,i)+0,'translation',opti,metric);
55             crop_trans_M(:,:,i)=crop_transformation.T;
56         end
57         %%Negative number because imregtform has strange coordinate system
58         dia_movement= -squeeze(crop_trans_M(3,2,:));
59
60         %% Plot commands
61         % See image processing result
62         % hold off
63         % for i=1:ZZ
64         %     subplot(1,ZZ,i)
65         %     imshow(X_crop(:,:,i),[])
66         % end
67         %pause()
68         %
69         % scatter(0:ZZ-1, squeeze(-crop_trans_M(3,2,:)))
70
71
72     end
73     %%

```

## B.6 Analysis programs

### Calculate spread of redundant images

```
1 function [percent_values,maximum_spread,spread_std]=SpreadCal(spread_type)
2
3 %% Plot intra bin spread and extract maximum and show percentage
4 global num pha num_slc
5 % * Here the conversion to mm is done
6 spread_range=zeros(num pha,num_slc);
7 spread_std= NaN(num pha,num_slc);
8 color_str= 'rb';
9
10
11     for b=1:num pha
12         for s=1:num_slc
13             %subplot(2,5,b)
14             if isempty(spread_type{b,s})==1
15                 continue
16             elseif isempty(spread_type{b,s})==1
17                 continue
18             end
19             % *
20             spread_l=spread_type{b,s}*0.78;
21             spread_range(b,s)=abs(max(spread_l))+abs(min(spread_l));
22             spread_std(b,s)= std(spread_l);
23             bin_val= repmat(s,[1 length(spread_l)]);
24             %
25             %     scatter(bin_val,spread_l,[],color_str(m))
26             %     title(sprintf('Bin%d',b))
27             %     xlabel('Slices')
28             %     ylabel('Variation (mm)')
29             %     ylim([-20 20])
30             %     hold on
31             close all
32         end
33     end
34     x_values=1:50;
35     percent_values=1:50;
36     for i=1:length(x_values)
37         x_values(i+1) = x_values(i)+0.5;
38         percent_values(i)=1-length(find(spread_range>x_values(i)))/(num pha*num_slc);
39     end
40
41     maximum_spread=0;
42
43     if maximum_spread< max(max(spread_range))
44         maximum_spread= max(max(spread_range));
45     end
46 end
```

## Stack images and create respiratory correlated GIF

```
1 function [diafragma_save_path]= StackAndGif(impath,raw_slicenum,dataname)
2 %% Extract image from each bin at slice=raw_slicenum
3 global num_slc
4 bins= 1:10;
5 respiratory_dirname= 'Respiratorysignal';
6 resp_path= fullfile(impath,respiratory_dirname);
7 dia_foldername=sprintf('slicenum%0.2d',raw_slicenum);
8 mkdir(resp_path,dia_foldername);
9 diafragma_save_path = fullfile(resp_path,dia_foldername);
10 dia_series= dicomuid;
11 count= 1;
12 slice_loc_dum=1;
13
14 for b= bins
15     h=waitbar(b/10,sprintf('Percentage of bins StackandGif from slice ...
16         %d/%d ',raw_slicenum,num_slc));
17     bin_load_path = fullfile(impath,num2str(b));
18     imfiles1= fullfile(bin_load_path,'*.dcm');
19     imstot = dir(imfiles1);
20     for i= 1: length(imstot)
21         slice_number= str2double(imstot(i).name(6:9));
22         if slice_number == raw_slicenum
23             d_image_name= fullfile(bin_load_path,imstot(i).name);
24             im = dicomread(d_image_name);
25             %Adaptive metadata to make sagital reconstruction possible
26             metadata= dicominfo(d_image_name);
27             metadata.SeriesInstanceUID= dia_series;
28             metadata.ImagePositionPatient(2) = ...
29                 metadata.ImagePositionPatient(2) + count;
30             instance_num= slice_loc_dum;
31             metadata.InstanceNumber=instance_num;
32             slice_loc_dum= slice_loc_dum +1 ;
33             count=count+1;
34             d_sav_name= imstot(i).name;
35             d_sav_name= fullfile(diafragma_save_path,d_sav_name);
36             dicomwrite(im,d_sav_name,'CreateMode','Copy',metadata);
37         end
38     end
39     close(h);
40 end
41
42 %% Change the slice location for each image (to keep order correct and ...
43     for sagital reconstruction)
44 imfiles= fullfile(diafragma_save_path,'*.dcm');
45 imstot = dir(imfiles);
46 count= 1;
```

```

46
47 for i= 1: length(imstot)
48     image_name= fullfile(diafragma_save_path,imstot(i).name);
49     image= dicomread(image_name);
50     metadata= dicominfo(image_name);
51     metadata.ImagePositionPatient(2) = ...
        metadata.ImagePositionPatient(2) + count;
52     dicomwrite(image,image_name,'CreateMode','Copy',metadata);
53     count= count+1;
54 end
55
56
57
58 %% Make gif from created slice num
59
60 gifname= ...
        fullfile(diafragma_save_path,sprintf('%s_slice%0.4d.gif',dataname(1:4),raw_slicenum));
61
62 for i=1:length(imstot)
63     filename = fullfile(diafragma_save_path,imstot(i).name);
64     X(:,:,i)= dicomread(filename);
65 end
66
67
68 for i = 1:length(imstot)
69     imshow(X(:,:,i),[]);
70     frame=getframe(1);
71     ImAndFrame = frame2im(frame);
72     [A,map] = rgb2ind(ImAndFrame,512);
73     if i == 1;
74         imwrite(A,map,gifname,'gif','LoopCount',Inf,'DelayTime',0.3);
75     else
76         imwrite(A,map,gifname,'gif','WriteMode','append','DelayTime',0.3);
77     end
78 end
79 end

```

### Compare phase binning and amplitude binning on diaphragmatic motion

```

1 function [diamove,dia_bins,pos_tocropPSlc] = ...
        CompareMethods(amplitude_dir ,phase_dir,pos_tocropPSlc)
2
3 %% Collect data to compare amplitude & phase binning and simple & ...
        average slice selection
4
5 % Compare simple & average just from phase binning
6
7 average_dir =     'Median selected 4D-MRI';
8 respsig_dir=     'Respiratorysignal';
9 global num_slc

```

```

10
11 bin_method = {'ampli','phase',};
12
13
14
15 %% Simple & average extraction for phase and amplitude binning
16
17 %%%%%%%%%%%%%%%%%%%%%%%%%%%%%%%%%%%%%%%%%%%%%%%%%%%%%%%%%%%%%%%%%%%%%%%%%%% SIMPLE IS COMENTED OUT%%%%%%%%%%%%%%%%%%%%%%%%%%%%%%%%%%%%%%%%%%%%%%%%%%%%%%%%%%%%%%%%%%%%%%%%%%
18
19 for bm=1:length(bin_method)
20     bins_slices= cell(num_slc,1);
21     if strcmp(bin_method(bm),'ampli')==1
22         bin_dir = amplitude_dir;
23     elseif strcmp(bin_method(bm),'phase')==1
24         bin_dir = phase_dir;
25     end
26     % simple_path= fullfile(bin_dir,simple_dir);
27     average_path= fullfile(bin_dir,average_dir);
28
29 %Per each bin 1 slice
30     for s=1:num_slc
31         h2=waitbar(s/num_slc,sprintf('Compare methods binning method: ...
32             %d/2',bm));
33         % X.simp=uint16([]);
34         X.avg= uint16([]);
35         name_resp_signal= sprintf('slicenum%0.2d',s);
36         avg_respSig_path = ...
37             fullfile(average_path,respSig_dir,name_resp_signal,'*.dcm');
38         % simple_respSig_path = ...
39             fullfile(simple_path,respSig_dir,name_resp_signal,'*.dcm');
40         % imstot_simp = dir(simple_respSig_path);
41         imstot_avg = dir(avg_respSig_path);
42
43         for im=1:length(imstot_avg)
44             im_avg = ...
45                 fullfile(average_path,respSig_dir,name_resp_signal,imstot_avg(im).name);
46         % im_simple= ...
47             fullfile(simple_path,respSig_dir,name_resp_signal,imstot_simp(im).name);
48         %Simple missing bin is always the same as the average missing
49         %bin!
50         bins_slices{s}(im)= str2double(imstot_avg(im).name(14:17));
51         % X.simp(:,:,im)= dicomread(im_simple);
52         X.avg(:,:,im)= dicomread(im_avg);
53     end
54
55     if isempty(pos_tocropPSlc{s})==1
56         [~,pos_tocropPSlc{s}]=imcrop(X.avg(:,:,1),[]);
57     end
58     if strcmp(bin_method(bm),'phase')==1
59         dia_bins.phase= bins_slices;

```

```

55 %         diamove.phase(s).sim = rigidReg('change func ...
rigid',X.simp,pos_tocropPSlc{s});
56         diamove.phase(s).avg = rigidReg('change func ...
rigid',X.avg,pos_tocropPSlc{s});
57     elseif strcmp(bin_method(bm),'ampli')==1
58         dia_bins.ampli= bins_slices;
59 %         diamove.ampli(s).sim = rigidReg('change func ...
rigid',X.simp,pos_tocropPSlc{s});
60         diamove.ampli(s).avg= rigidReg('change func ...
rigid',X.avg,pos_tocropPSlc{s});
61     end
62     close(h2)
63 end
64 end
65
66
67 end

```

### Calculate diaphragmatic shape in each bin

```

1 function [continuity_dia,pos_tocrop]= ...
    calcOrganDiscontinuity(avg_save_path,pos_tocrop)
2
3
4
5 %% Organ discontinuity
6 global num pha num_slc
7 continuity_dia=cell(num pha,1);
8 for b=1:num pha
9     X=uint16([]);
10    images_path= fullfile(avg_save_path,num2str(b));
11    imstot= dir(fullfile(images_path,'*.dcm'));
12    for i=1:length(imstot)
13        im_name= imstot(i).name;
14        X(:,:,i)= dicomread(fullfile(images_path,im_name));
15    end
16    % counter wrong pos_tocrop
17    if length(pos_tocrop)<num_slc+2
18        msgbox('Select diaphragm for discontinuity analysis')
19        [~,pos_tocrop{num_slc+2}]= imcrop(X(:,:,6),[]);
20    elseif isempty(pos_tocrop{num_slc+2})==1
21        msgbox('Select diaphragm for discontinuity analysis')
22        [~,pos_tocrop{num_slc+2}]= imcrop(X(:,:,6),[]);
23    end
24
25
26    pos= pos_tocrop{num_slc+2};
27    continuity_dia{b} = rigidReg('changefunc',X,pos);
28 end

```